UNIVERSITY OF CALIFORNIA, SAN DIEGO

Vanadium oxide phase transitions: fast, small, and strained

A dissertation submitted in partial satisfaction of the
requirements for the degree Doctor of Philosophy

in

Physics

By

Ilya Valmianski

Committee in charge:

Professor Ivan K. Schuller, Chair
Professor Massimiliano Di Ventra
Professor Shaya Fainman
Professor Shayan Mookherjea
Professor Oleg Shpyrko

2017

The Dissertation of Ilya Valmianski is approved, and it is acceptable in quality and form for publication on microfilm and electronically:

_____

_____

_____

_____

_____

Chair

University of California, San Diego

2017

DEDICATION

To the frogs and the owls

TABLE OF CONTENTS

LIST OF FIGURES

ACKNOWLEDGEMENTS

My path towards completing this PhD was long and circuitous. Through help and in collaboration with a multitude of wonderful people I was able to try myself with many different problems and in different fields. I am glad that in the end I worked in condensed matter physics experiment, it has made me an ever more rounded person and helped shape my perspective of physics and the world around me. In guiding me thought this journey, I would like to thank first and foremost my advisor, Prof. Ivan Schuller. His patience, advice, and creativity taught me a lot not only about physics, but also about working with collaborators, presenting my ideas in front of others, and developing new projects. Prof. Schuller is a man of vision and kindness and I am honored to be his student.

This journey would also be impossible without my parents – Olga Valmianskaya and Emanuil Valmianski. They have sacrificed enormously to bring me to the US. The opportunities afforded to me in this country are countless and I am forever thankful to be here. While my mother has passed away and cannot be here with me, her encouragement and vision of my future drives me forward. I am also very grateful to my father who has raised me and shaped the man that I have become. His invaluable advice and insights helped me see problems from many different angles and augmented my own judgement. I think much of my success is due to my excellent upbringing and my parents' support of my pursuits.

I would like to extend a special thank you to Dr. Carlos Monton. When I joined the Center for Advanced Nanoscience, he was my mentor and introduced me to many ideas and techniques that I would later use throughout my PhD. I have learned much of

what I know about vacuum systems and working with complex equipment from him. He has always been very encouraging of me and we worked great as a team in our projects on phthalocyanines and porous alumina. Both of us were able to bring together our strengths to do very good work. Our collaboration was very fruitful and produced eight papers.

I would like thank people who have taught me to use the many different experimental techniques. I would like to thank Dr. Yaniv Rosen and Dr. Siming Wang for teaching me much of what I know about physical vapor deposition and nanodevice fabrication as well as making electrical measurements. These were the primary tools of my PhD research. I would like to thank Dr. Gabriel Ramirez for teaching me a lot about sensitive electrical measurements and magnetism. Finally, I would like to thank Dr. Jose de la Venta and Dr. Thomas Saerbeck for teaching me a lot about scattering. With their guidance I learned many X-ray techniques and has since been able to pass along the "know how" to newer members of the group. Many of the measurement modalities introduced to our group with the purchase of the new X-ray system and the hard work of Dr. Saerbeck have benefited me in almost every project in which I participated.

I would like to thank many of my collaborators. In my group, I worked most closely with Dr. Carlos Monton, Dr. Gabriel Ramirez, Dr. Siming Wang, and Dr. Christian Urban. Their work was important in completing the many projects I was involved in and produced 17 papers. I also had a very productive collaboration with an undergraduate student, Paul Wang, he is a truly talented individual and I am sure he will have much success in his future scientific endeavors. I had many great collaborations outside of my group with many dozens of people involved. At UCSD particularly

interesting was my work with Dr. Andrej Singer and Dr. Oleg Shpyrko. Our work on fast X-ray pump probe of V_2O_3 forms the third chapter of my dissertation. At UCSB, I made good work with Nikita Butakov and Dr. Jon Schuller. Our work on vanadium oxide based tunable metamaterials produced two papers and is a truly exciting area of research.

I would also like to thank individuals who have sparked my aptitude for research and scientific inquiry. My first serious project came during my internship at General Atomics under the mentorship of Dr. Richard Stefens when I was just a high school student. Our work resulted in a publication in Fusion Science and Technology. Another person who made a great impact on me is Dr. David Kleinfeld, who I met during my undergraduate years. I published my first first-author paper with him and I am very grateful for all the guidance and support he has given me.

Finally, I would like to thank all of the group members who generated the creative environment which was my work. I would like to thank especially Dr. Christian Urban and James Wampler for many hours of discussion and debate, which enriched my understanding of physics and the world. I would also like to thank my many friends outside of my research group. In particular, Jason Leonard, Rhiannon Kennard, Ben Holladay, and Zihan Xu have all been instrumental in my success though the many trials and tribulations I have experienced. Their help, guidance, and humor have colored my life.

Chapter 1 was in part prepared using a publication: Ilya Valmianski, Carlos Monton, Ivan K. Schuller, " Microscopy Image Segmentation Tool: Robust image data analysis", Review of Scientific Instruments, 85:3 (2014). The dissertation author was the primary investigator and author of this paper.

Chapter 2 was prepared based on a paper that is to be submitted with the following author list: Andrej Singer, Juan Gabriel Ramirez, Ilya Valmianski, Devin Cela, Nelson Hua, Roopali Kukreja, James Wingert, Olesya Kovalchuk, James M. Glownia, Marcin Sikiroski, Matthieu Chollet, Martin Holt, Ivan K. Schuller, and Oleg G. Shpyrko. A.S and J.G.R. conceived of the idea. A.S., J.G.R., I.K.S., and O.G.S planned the experiment. J.G.R. and I.V. prepared the samples and performed resistance measurements for in-situ calibration. A.S, J.G.R, I.V., D.C, N.H., R.K., O.K., J.M.G., M.S., M.Ch., and O.G.S. conducted the time resolved experiment. A.S., N.H., J.W., and M.H. conducted the nanodiffraction experiment. A.S. analyzed the data. All authors discussed the interpretation of the data. A.S., J.G.R., and I.V. wrote the paper with input from all authors. The dissertation author was a major contributor to this paper.

Chapter 3 was prepared based on a paper that is to be submitted with the following author list: Ilya Valmianski, Siming Wang, Paul Wang, Juan Gabriel Ramirez, Stefan Guenon, Ivan K. Schuller. S.W, S.G., J.G.B. and I.K.S conceived of the idea. S.W, S.G., and I.V. prepared the samples and performed resistance measurements. I.V. and P.W. analyzed the data and proposed the theoretical model. All authors discussed the interpretation of the data. I.V., J.G.R., and P.W wrote the paper with input from all authors. The dissertation author was the primary investigator and author of this paper.

Chapter 4 is a reproduction of the paper Ilya Valmianski, Juan Gabriel Ramirez, Christian Urban, Xavier Batlle, and Ivan K. Schuller “Deviation from bulk in the pressure-temperature phase diagram of V2O3 thin films” Phys. Rev. B 95, 155132 (2017). I.V, J.G.B, and C.B fabricated and measured all samples. I.V. performed the

analysis of the data. I.V. and J.G.B. wrote the paper with input from all authors. The dissertation author was the primary investigator and author of this paper.

Apprendix B was published as supplemental material for the paper Ilya Valmianski, Juan Gabriel Ramirez, Christian Urban, Xavier Batlle, and Ivan K. Schuller "Deviation from bulk in the pressure-temperature phase diagram of V2O3 thin films" Phys. Rev. B 95, 155132 (2017). The dissertation author was the primary investigator and author of this paper.

VITA

Education

2009 – 2017
Doctor of Philosophy, Physics — University of California, San Diego

2009 – 2010
Master of Science, Physics — University of California, San Diego

2005 – 2009
Bachelor of Science, Physics-Biophysics — University of California, San Diego

Publications

1. C. Urban, **I. Valmianski**, U. Pachmayr, A. C. Basaran, D. Johrendt, Ivan K. Schuller, "Competition of superconducting and structural length scales in lithiated iron selenide hydroxide [(Li1-xFex)OH]FeSe" (Manuscript in revision, Phys Rev B)
2. N. A. Butakov, **I. Valmianski**, T. Lewi, C. Urban, Z. Ren, A. A. Mikhailovsky, S. D. Wilson, Ivan K. Schuller, J. A. Schuller, "Switchable Dielectric-Plasmonic Resonators with Insulator-Metal Transitions" (Manuscript in revision, ACS Photonics)
3. **I. Valmianski**, J. G. Ramirez, C. Urban, X. Battle, I.K. Schuller, "Deviation from bulk in the pressure-temperature phase diagram of V_2O_3 thin films", Physical Review B 95:15 (2017)
4. S. Finizio, M. Vafaee, **I. Valmianski**, R. M. Reeve, R. L. Conte, A. Kleibert, Ivan K. Schuller, M. Kläui " Control of the Magnetic Configuration of Ferromagnetic Nanostructures Across the Structural Phase Transition of Vanadium Dioxide", IEEE Magnetics Letters, 6 (2016)
5. C. Urban, A. Quesada, T. Saerbeck, M. A. Garcia, M. A. De la Rubia, **I. Valmianski,** J. F. Fernández, Ivan K Schuller, "Two state coercivity driven by phase coexistence in vanadium sesquioxide/nickel bulk hybrid material", Applied Physics Letters 109:11 (2016)
6. Y. Tian, A. A. Reijnders, G. B. Osterhoudt, **I. Valmianski**, J. G. Ramirez, C. Urban, R. Zhong, J. Schneeloch, G. Gu, I. Henslee, K. S Burch , "Low vibration high numerical aperture automated variable temperature Raman microscope" Review of Scientific Instruments, 87:4, (2016)
7. A. Serrano, O. Rodriguez de la Fuente, C. Monton, A. Munoz-Noval, **I. Valmianski**, J. Fernandez Lozano, G. R. Castro, I.K. Schuller, M. Garcia "Effect of X-ray irradiation on Co-phthalocyanine thin films studied by Surface Plasmon Resonance", Journal of Physics D, 49:12 (2016)
8. S. P. Bennett, A. Wong , A. Glavic , A. Herklotz , C. Urban, **I. Valmianski** , M. Biegalski , H. Christen , T. Ward , V. Lauter, " Giant Magnetization Switching

Induced by Structural Phase Transitions in a Metamagnetic Artificial Multiferroic", Sci Rep. ; 6: 22708 (2016)
9. F. Golmar, P. Stoliar, C. Monton, **I. Valmianski,** I. K. Schuller, L. E. Hueso, F. Casanova, "Cobalt phthalocyanine-based submicrometric field-effect transistors" Physica Status Solidi A, 212:3 607, (2015)
10. T. Saerbeck, J. de la Venta, S. M. Wang, J. G. Ramirez, M. Erekhinsky, **I. Valmianski**, I. K. Schuller, "Coupling of magnetism and structural phase transitions by interfacial strain" Journal of Materials Research, 29:20 2353 (2015)
11. **I. Valmianski**, C. Monton, I. K. Schuller, " Microscopy Image Segmentation Tool: Robust image data analysis", Review of Scientific Instruments, 85:3 (2014)
12. A. Serrano, C.Monton, **I. Valmianski**, J. de la Venta, Ivan K. Schuller, M.A. Garcia, "Study of Co-Phthalocyanine films by Surface Plasmon Resonance spectroscopy: Whole curve analysis", J. of Appl. Phys. 115, 103106 (2014);
13. J. de la Venta, S. Wang, T. Saerbeck, J. G. Ramírez, **I. Valmianski**, Ivan K. Schuller, "Coercivity enhancement in V2O3/Ni bilayers driven by nanoscale phase coexistence", Appl. Phys. Lett. 104, 062410 (2014)
14. C. Monton, T. Saerbeck, **I. Valmianski**, Ivan K. Schuller, "Charge injection across a metal-organic interface suppressed by thermal diffusion". Appl. Phys. Lett. 104, 043301 (2014)
15. T. Willey, M. Bagge-Hansen, J. R. I. Lee, R. W. Call, L. Landt, A. van Buuren, C. Colesniuc, C. M. Monton, **I. Valmianski**, and I. K. Schuller, "Electronic Structure Differences Between H_2-, Fe-, Co-, and Cu-Phthalocyanine Highly Oriented Thin Films Observed Using NEXAFS Spectroscopy", J. Chem. Phys. 139 (3) (2013)
16. C. Monton, **I. Valmianski** and I. K. Schuller, " The role of micro-shorts and electrode-film interface in the electrical transport of ultra-thin metallophthalocyanine capacitive devices " Appl Phys Lett 101 (13) (2012).
17. F. Galvez, C. Monton, A. Serrano, **I. Valmianski**, J. de la Venta, I. K. Schuller and M. A. Garcia, "Effect of photodiode angular response on surface plasmon resonance measurements in the Kretschmann-Raether configuration." Review of Scientific Instruments 83 (9) (2012).
18. **I. Valmianski**, A. Y. Shih, J. D. Driscoll, D. W. Matthews, Y. Freund and D. Kleinfeld, " Automatic identification of fluorescently labeled brain cells for rapid functional imaging" J Neurophysiol 104 (3), 1803-1811 (2010).
19. H. Huang, R. B. Stephens, J. B. Gibson and **I. Valmianski**, "3D surface reconstruction of ICF shells after full surface spheremapping " Fusion Sci Technol 49 (4), 642-645 (2006).

ABSTRACT OF THE DISSERTATION

Vanadium oxide phase transitions: fast, small, and strained

By

Ilya Valmianski

Doctor of Philosophy in Physics

University of California, San Diego, 2017

Professor Ivan K. Schuller, Chair

Vanadium oxides are a prototypical family of highly correlated oxides. In his dissertation, I present the study of two vanadium oxides in particular, V_2O_3 and VO_2, which undergo simultaneously both a structural phase transition and a metal to insulator

transition. While traditionally these phase transitions were studied in equilibrium, bulk, or in meso/macro-scale devices, in my work I focused on different modalities: fast, small, and strained.

In my work on fast time scales during photoexcitation of V_2O_3 we found a novel meta-stable intermediate state that appears due to symmetry change in the monoclinic phase. This change occurs in the proximity of high temperature rhombohedral domains on length scales similar to those of electronic correlation. Our finding shows that the electronic and structural transitions in V_2O_3 have similar length scales but very different time scales.

In VO_2 and V_2O_3 nanoscale devices, we found a length-scale competition between Joule heating and electric field driven current induced metal to insulator transition. We proposed a novel thermoelectric model and performed simulations using finite element methods. Our modeling showed that the transition is highly inhomogeneous and the resulting filaments are surface bound with thermal gradients generating Seebeck electric fields on the order of 1000 V/cm.

Finally, we studied pressurized and strained thin films in V_2O_3 and discovered strong strain relaxation for pressures of up to 500 MPa, which cause a deviation of thin film Pressure-Temperature phase diagram from bulk behavior. This strain relaxation relies on the difference between the structural and morphological length scales, which allows the formation of strain relaxing creases. Once those creases are fully strained, the thin films respond similarly to bulk samples.

Chapter I - Introduction

1.1 Overview

Correlated metal oxides form an exciting material class. They present many unusual electrical[1–5], optical[6–8], structural[9–12] and magnetic[13–15] properties that are not only hard to predict but even to explain. Many novel behaviors, such as high temperature superconductivity[16,17], colossal magnetoresistance[18], topologically protected phases[19–21], spin liquids[22], metal to insulator transitions[1,23], and Mott insulators[24] have been found in metal oxides. The richness of electronic properties makes these materials a perfect playground for experimental condensed matter, where novel techniques allows us to probe properties at ever-smaller length scales and faster times revealing the underlying physical processes. At the same time, metal oxides are considered for many important applications such as photovoltaics[25,26], photocatalytics[26–28], tunable metamaterials, atomic-scale FETs[29], neuromorphic devices[30–32], and quantum computing[33].

An important family of correlated metal oxides are the vanadium oxides, whose members exhibit metal insulator transitions, antiferromagnetism, Mott insulator states, and other interesting properties[12,23,34,35]. In my thesis work, I focused on two materials from this family – vanadium dioxide (VO_2) and vanadium sesquioxide (V_2O_3). While their macroscopic phenomenological properties are very similar, probing the materials at short length scales and fast time scales reveals a difference in the underlying physics of the two systems. Primarily, my work is focused at looking at the electrical transport and structure; however, through collaborations with outside groups I also examined optical and magnetic behaviors. Furthermore, for V_2O_3, I performed detailed studies of thin films under strain and mechanically coupled to magnetic materials. It was found that both

the strain response and the mechanical coupling is different in thin films and bulk materials and heterostructures.

1.2 VO_2 and V_2O_3 Metal-Insulator and Structural Transitions

One of the most striking behaviors of the vanadium oxides is the presence of the Metal-Insulator Transition (MIT). Originally discovered over half-century ago, it is an electronic first order phase transition that always co-occurs with a structural phase transition (SPT). These transitions feature a strongly hysteretic behavior with a wide co-existence region. For applications, this makes them interesting for bi-stable, elastically coupled, and memristive systems. A key question about the physics of these transitions is whether the structural or the electronic transition drives the phase change.

The Magneli sequence of Vanadium Oxides, characterized by V_nO_{2n-1} stoichiometry, all possess the MIT at various temperatures[36]. The two extremes of the sequence are VO_2 ($n = \infty$) and V_2O_3 ($n = 2$). In VO_2, the SPT is characterized by dimerization of the vanadium atoms in a Peierls-like structural transition from high temperature metallic rutile to low temperature insulating monoclinic symmetry at ~330 K. However, recent theoretical work suggests that on-site interaction play at least part of the role, suggesting a spin-Peierls or partial Mott nature[37]. In V_2O_3, the transition is considered to be electronically driven with vanadium atoms forming long antiferromagnetic chains while transitioning from the high temperature metallic rhombohedral phase to low temperature insulating monoclinic phase at ~160 K[38]. While the classical Mott transition occurs in V_2O_3 at high negative pressures achieved through

chromium doping, the transition my work focused on is in the positive pressures regime between the antiferromagnetic insulator and paramagnetic metal[39,40].

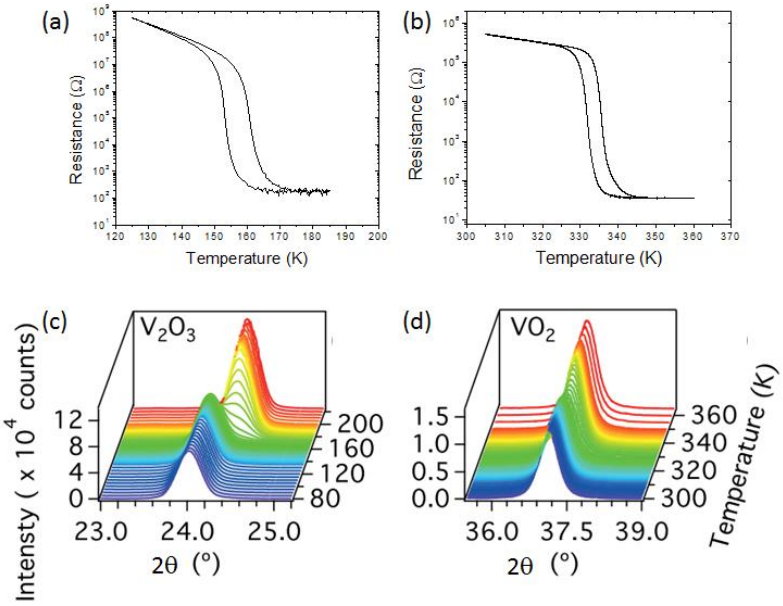

Figure 1.1: Metal to insulator and structural transitions in V_2O_3 and VO_2. Resistance vs temperature curves of (a) V_2O_3 and (b) VO_2. Out of plane x-ray diffraction peak as a function of temperatures for (c) V_2O_3 and (d) VO_2. Adapted from [41]

Both VO_2 and V_2O_3 show a hysteretic resistance versus temperature curve (Figure 1.1). The transition width is typically 5 to 10 K wide and the resistance change is 3 to 5 orders of magnitude (Figure 1.1a, b). Transition temperatures and magnitude as well as hysteresis shape can be adjusted though choice of substrate or deposition conditions. The film properties are sensitive to the out of plane crystallographic orientation, oxygen content, and interfacial morphology[42]. Because both the rutile and rhombohedral phases have higher symmetries than the monoclinic phase, twinning occurs when the material is cooled below the transition temperature[12,43]. This explains why low temperature peaks in Figure 1.1b,c are lower intensity than the higher temperature peaks. Twinning lengthscale

may also be related to electronic coherence length in the material, as the two numbers are coincident at least in V_2O_3[44].

While the twinning occurs in both vanadium oxides on the few nanometer length scales, nearfield infrared spectroscopy[45], X-ray nanodiffraction, and low temperature conductive SEM[46] measurements reveal a phase separation on the length scales on the order of 100 nm. This suggests that length scales longer than twinning play an important role in both SPT and MIT. Irradiation experiments reveal that low levels of disorder can rapidly suppress the V_2O_3 but not VO_2 transition[47]. Furthermore, studies of avalanches in the resistance during the MIT suggests that V_2O_3 percolative process is correlated while the VO_2 percolative process is random switching[48].

All of this sets up many interesting questions about the lengthscales of the MIT and SPT in vanadium oxides. Despite many similarities in macroscopic observables, there are clear differences in microscopic observables. By looking at this small scales as well as short time scales and strain we try to shine light on the differences between VO_2 and V_2O_3. In chapter II, I examine the fast-time scale behavior of SPT in V2O3 and its connection to the short length-scale twinning. In chapter III, I will discuss DC electrical measurements in small length scale VO_2 and V_2O_3 where we show that we can induce both a thermally and electrically driven MIT. In Chapter IV, we discuss a collaboration where we show switchable optical driven by VO_2 MIT. In chapter V, we discuss the differences in strain response between bulk and thin film V_2O_3 films, which are due to nanoscale morphology in the films. Finally, in chapter VI, I show the nanoscale effect of SPT elastically coupling in a V_2O_3-Ni magnetic heterostructures.

1.3 Experimental procedures

1.3.1 V_2O_3 thin film growth

The V_2O_3 films were prepared by reactive magnetron sputtering on Al_2O_3 from both in house and commercially produced V_2O_3 targets. The commercial targets were sourced from AC Alloys and Plasmamaterials. Both companies do not perform structural analysis and do not guarantee target quality, only elemental purity. The homemade target was manufactured by pressing Noah Technologies 99.9% purity V_2O_3 powder followed by a 15 hours sintering process under Ar/H(2%) atmosphere at 1050 ^{o}C. Homemade targets were selected for structural purity, however, even the most structurally pure targets had densities lower than commercial targets. Target density did not play a big role in thin film quality, although homemade targets tended to result to slightly faster deposition rate.

The sputtering was performed in a high vacuum system (base pressure of 1×10^{-7} Torr) backfilled with ultrahigh purity (UHP-99.999%) Ar gas in a Microscience chamber (Microscience I). Majority of the films were made in the non-cluster guns, at the 10 mm position. The backfilled gas pressure was 4 mT. Higher pressures (up to 8 mT) corresponded to better film smoothness but smaller MIT resistance change. Above 8 mT, the film smoothness deteriorated. Below 4 mT the deposition rate, film smoothness, and size of the MIT were worse. Some films were deposited from the cluster guns, at which point the confocal height was used as well as higher backfill pressure (8 mT) although typical deposition times increased (45 min – 1 hour for 100 nm vs 15-30 min in single gun).

Deposition was done using RF sputtering source at 100 W at the power supply. Typically the matching network was able to deliver 90 W to the plasma with about 5 W being reflected. Often sparking the plasma required a second DC power supply to be turned on with a metallic target. The matching network automatic capacitor adjustment often led to saturation of one of the capacitors, which could be corrected by turning the matching network to manual mode and then returning it back to the automatic operation.

For both cluster and non-cluster gun configurations the heater thermocouple was set to 1000 ^{o}C, which corresponds to 750 ^{o}C substrate temperature. Higher temperature would potentially benefit thin film quality, however the tungsten lamps in the heater had rapid burn out at temperatures above 1000 ^{o}C. The heater was rapidly turned on from RT to 200 ^{o}C and then further heating was done at 12 ^{o}C/min. Once the temperature reached the goal the substrate was kept at a fixed temperature for 30 min. A 10 min pre-sputtering was performed. Once the deposition was complete, the film was cooled down to 200 ^{o}C at the 12 ^{o}C /min rate while in constant Ar atmosphere.

Al_2O_3 orientation plays an important role in film quality. While all orientations produce epitaxially structure V_2O_3, orientation plays a significant role in the width, height, position, and shape of the R-T hysteresis loop of the MIT. For the above mentioned conditions highest quality films were produced on r-plane. Films deposited on the m-plane showed similarly sized and shaped transitions but at a higher transition temperature (170 K vs 160 K), while films grown on a-plane showed much smaller and wider transition as well as a larger amount of polycrystalline rings in the film (see Chapter 5). Films grown on c-plane showed almost no transition but this may be due to surface morphology produced by Al_2O_3 terracing in this orientation.

1.3.2 VO_2 thin film growth

The VO_2 films were prepared by reactive magnetron sputtering on r-plane oriented Al_2O_3 in a similar fashion to the V_2O_3 films (section 1.3.1). The sputtering was performed in the same chamber as V_2O_3 films from the same V_2O_3 target in a single gun configuration. The chamber was backfilled with 4 mTorr ultrahigh purity (UHP-99.999%) Ar/O(8.5%) gas mixture (2.3 sccm of Ar, 1.7 sccm of Ar/O(20%)). The heater temperature was kept at 760 ^oC, corresponding to substrate temperature of 600 ^oC. The heating was performed with 12 ^oC/ramp. Lower deposition temperatures led to worse

When starting VO_2 growth after V_2O_3/metallic growths it is important to condition the chamber. Typically conditioning was 1-2 hours at 100 W RF power, with the substrate holder present over the gun to be coated. Before each deposition a pre-sputtering of 30 min was performed. The deposition times for VO_2 were longer than for V_2O_3, typically 45 min – 1 hour for 100 nm, due to back sputtering by O^{2-} ions. The films are highly textured with the (300) monoclinic in VO_2 direction coinciding with the (012) direction in the substrate and also oriented in the in-plane. This is likely due to a V_2O_3 like interfacial layer that forms at the VO_2/Al_2O_3 interface due to vanadium cation dislocations[49].

1.3.3 X-ray measurements

Thin film, bulk sample, and sputtering target characterizations were performed using x-ray measurements on Rigaku Smartlab Tube Diffractometer and Bruker D8-Discover Rotating Anode Diffractometer. Types of analysis performed were x-ray reflectivity, low angle diffuse scattering, rocking curve measurements, out-of-plane and in-plane x-ray diffraction, pole figures, and two types of reciprocal space mapping.

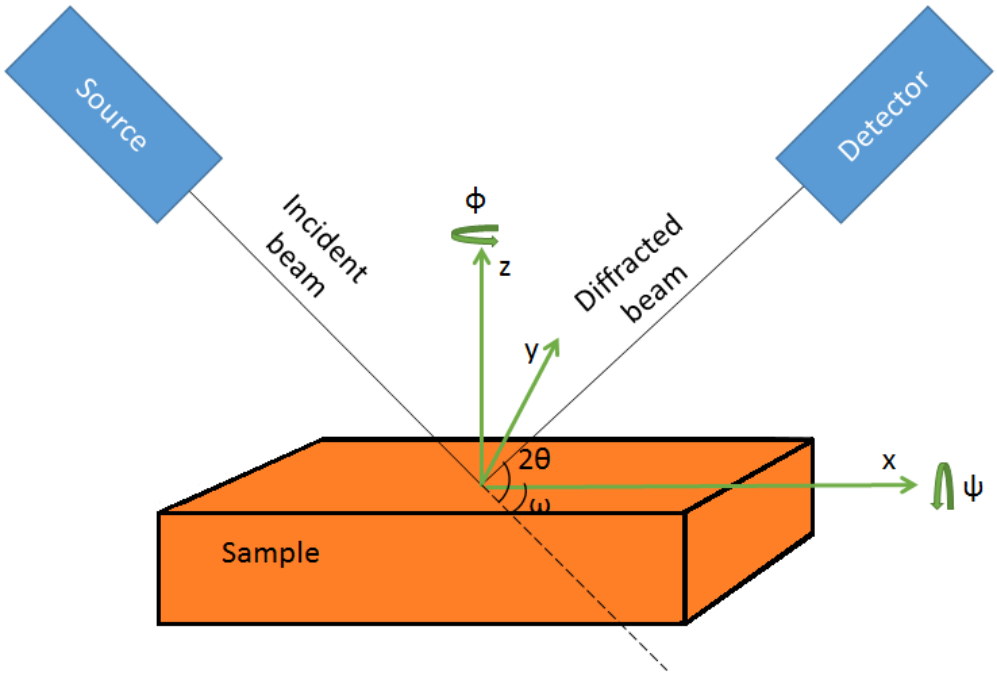

Figure 1.2: Schematic of the x-ray diffractometer geometry

The Rigaku Diffractometer was normally operated at 40 kV/44 mA voltage/current setting. The optical path consists of a choice of 2 bounce (220) Ge monochrometer or 5 degree Soller slits, one incident slit (IS), one incident length limiting slit, 2 receiving slits (RS1 and RS2), and receiving 5 degree Soller slits. In the standard (cradle) configuration φ, ψ, ω, and 2θ rotations are possible as well as z-axis translation (see Figure 1.2 for schematic of the geometry). An Anton Par low temperature stage (down to 130 K) was used for low temperature measurements, in which case phi and chi rotation were unavailable. Pre-built wedges were used to create chi offsets for in-plane measurements at low temperature. Both an automatic and manual modes of operation are available. While the automatic mode is more convenient and was the dominantly used mode, for low signal measurements the manual mode provided much more consistent alignment quality. All multiple scan measurements (reciprocal space maps and pole

figures) were done in the automatic mode. Low angle measurements (<5^o in 2-theta) were typically done with 0.1 mm/0.1 mm/0.1 mm slit openings for (IS/RS1/RS2), while most diffraction measurements were done with 1 mm/1 mm/1.2 mm slit openings.

The Bruker Diffractometer was operated at 40 kV/200 mA voltage/current setting. Bruker specification suggest operating current of 300 mA, but this proved to be unrealistic due to high arcing rate. The optical path consists of a choice of 4 bounce (220) Ge monochrometer or 5 degree Soller slits, two incident slit (IS1 and IS2), 2 receiving slits (RS1 and RS2), and a receiving length limiting slit. In the standard (cradle) configuration phi, chi, omega, and two-theta rotations are possible as well as x-, y-, z-axis translation. The x- and y- translation are especially useful for small samples as it allows for optimizing the incident beam position. Most measurements were done in a manual configuration, although there is a macro batch job processors for automated scans. Low angle measurements (<5^o in 2-theta) were typically done with 0.1 mm/0.1 mm/0.1 mm/0.1 mm slit openings for (IS1/IS2//RS1/RS2), while most diffraction measurements were done with 1 mm/1 mm/1 mm/1.2 mm slit openings.

The alignment procedure for low angle measurements was the following:

1) At $\theta/2\text{-}\theta = 0^o$ perform a z-scan. This should produce a step function and the z should be fixed at the mid-point.

2) Perform rocking curve around 2-theta = 0^o. This should form a pyramid shape and the omega should be fixed at the peak.

3) Repeat steps 1) and 2) until the intensity converges.

4) Set 2-theta to a value slightly past critical edge (~0.6^{o} typically, but a 2-theta scan may be needed) and perform rocking curve. This should create a Voigt profile and the omega should be fixed at center of gravity of the profile.

5) Scan chi (typical range -5^{o} to 5^{o}), this should produce a pyramid shape and the omega should be fixed at the peak

6) Steps 4 and 5 can be repeated until the values converge. If there is significant change in omega offsets a z-scan may need to be repeated, in which case it should produce a peak at the correct alignment.

For high angle/diffraction measurements:

1) Perform z alignment same as in the low angle measurements.

2) Set 2-theta to the location of a known peak.

3) Perform a rocking curve. This should create a Voigt profile and the omega should be fixed at center of gravity of the profile.

4) Scan chi (typical range -5^{o} to 5^{o}), this should also create a Voigt profile and chi should be fixed at the “center of gravity” (intensity weighted mean).

5) Steps 3 and 4 should be repeated until both values converge.

6) Occasionally, phi dependence is present and doing a -5^{o} to 360^{o} can be used to find a region of higher intensity. After change phi, repeat steps 3-5.

When performing alignment, two indicators can be used to see if the sample is improperly aligned in the xy plane. If the z-scan produces multiple steps this means that part of the beam passes outside the sample on the y-axis. This can be corrected by improving the y-axis centering of the sample or reducing the length limiting slit size.

When performing rocking curve around 2-theta = 0^o occasionally the pyramid shape is asymmetric (one side is steeper than another). This is due to x-axis misalignment. This can be corrected by improving the x-axis centering of the sample or reducing the incident slit size. On Bruker Diffractometers, the xy stage motors can be used to perform x- and y-axis scans, as an alternative method for optimizing the xy position, which is especially useful for very small sample sizes (~1 mm^2).

Several in-plane measurement techniques were used. For pole figures, the XRD alignment was performed. The pole figure itself was measured using the pole figure macro in Rigaku. Because of poor chi resolution (divergence angle is defined by the length limiting slit), a 3^o step in chi is typical. Phi step of 0.1^o was typically used. For in-plane reciprocal space maps (chi steps), a custom macro was used. The program pseudocode is the following:

1) Perform XRD alignment on an out of plane peak and go to the initial ψ
2) Start FOR loop
3) Perform GENERAL MEASUREMENT for 2-theta/omega
4) Perform RELATIVE MOVE in chi
5) END FOR loop

For normal reciprocal space maps (omega steps), a prebuilt RSM macro in Rigaku was used. Typical omega and 2-theta steps were 0.1^o.

Anton Par low temperature stage for the Rigaku Diffractometer was used for measurement of temperature driven SPTs in V_2O_3 and FeRh samples. Ψ and φ angle rotations are unavailable in this configuration but wedges can be used to access in plane directions. Temperature controller can be programmed using Rigaku Diffraction

Controller prebuilt macros. In general, temperature sweeps can be setup using either regular for loops with relative temperature change macros or using the special temperature-for loop. Several custom program were made for diffraction, reflection, and diffuse scattering measurements as a function of temperature.

1.3.4 Reactive Ion Etching

Vanadium oxide regions of interests were defined using reactive ion etching. An etching process rather than a lift off process was using because life off leaves small pieces of resist on the surface even after oxygen cleaning leading to poor film quality. The primary reactive ion etching system used was Oxford Instruments P80. For 100 nm of V_2O_3, the etching was performed for 2 minutes under 40 mTorr pressure with 50 sccm Cl_2 and 10 sccm Ar flow at 200 W.

1.3.5 Photolithography

Positive photolithography using S1818 resist

1) Initial spin coating of for 10 s at 300 rpm.
2) Main spin coating for 1 min at 5000 rpm.
3) Backing at 115 °C on a hot plate for 1 min. The low temperature is critical to prevent VO_x degradation
4) 3.5 min UV exposure in SUSS MJB 3 mask aligner.
5) 40 s development in a mixture of 50 % AZ developer/50 % DI water.
6) 30 s deionized water rinse
7) Drying in high purity nitrogen

1.3.6 E-beam lithography

Positive e-beam lithography using 950 PMMA C4 and A2 resists

1) Initial spin coating of for 10 s at 300 rpm.

2) Main spin coating for 1 min at 3000 rpm.

3) Backing at 110 °C on a hot plate for 10 min. The low temperature is critical to prevent VO_x degradation

4) E-beam exposure using Raith 50 EBL at 30 kV acceleration voltage, 100 pA probe current. Typical doses 270 and 330 $\mu C/cm^2$.

5) 40 s development in 25 % MIBK and 75 % isopropanol

6) 30 s isopropanol rinse

7) Drying in high purity nitrogen

1.3.7 Microscopy Image Segmentation Tool

I have developed a software package called Microscopy Image Segmentation Tool (MIST). MIST is designed for analysis of microscopy images, which contain large collections of small regions of interest (ROI). Originally developed for analysis of porous anodic alumina scanning electron images, MIST capabilities have been expanded to allow use in a large variety of problems including analysis of biological tissue, inorganic and organic film grain structure, as well as nano- and meso-scopic structures. MIST provides a robust segmentation algorithm for the ROIs, includes many useful analysis capabilities, and is highly flexible allowing incorporation of specialized user developed analysis.

MIST uses a robust multistep segmentation algorithm which utilizes both per pixel intensity information as well as morphological filtering. The algorithm makes two assumptions about the underlying imaging data. First, MIST assumes that there is local but not necessarily global contrast between ROI and background. This means that significantly overlapped ROIs are not well segmented however changes in background

intensity across the image are corrected. Second, MIST assumes that ROI areas have a Gaussian-like distribution, which is true for most ROI types; however if the area distribution is multimodal (has many peaks), certain ranges of ROI sizes can be excluded.

The full segmentation algorithm is as follows. For an input image I:

1) Median filter pixel intensity using a 5 by 5 pixel window

2) Compute a locally normalized image $\tilde{I}_N$ using a window of size N

$$\left\langle I_{x,y} \right\rangle_N = \frac{1}{(N+1)^2} \sum_{i=x-N/2}^{x+N/2} \sum_{j=y-N/2}^{y+N/2} I_{i,j}$$

$$\left\langle \sigma_{x,y} \right\rangle_N = \sqrt{\frac{1}{(N+1)^2 - 1} \sum_{i=x-N/2}^{x+N/2} \sum_{j=y-N/2}^{y+N/2} \left(I_{i,j} - \left\langle I_{x,y} \right\rangle_N \right)}$$

$$\tilde{I}_{x,y,N} = \frac{I_{x,y} - \left\langle I_{x,y} \right\rangle_N}{\left\langle \sigma_{x,y} \right\rangle_N}$$

3) Compute the mean (μI) and standard deviation (σI) of intensities in $\tilde{I}_N$

4) Threshold $\tilde{I}_N$ at intensities ranging from μI - 3 σI to μI + 3 σI with a step size of 1/2 σI to produce thirteen black and white images BW_i.

5) Erode each BW_k with a 3x3 pixel square.

6) Compute the mean (μBW_i) and standard deviation (σBW_i) of the areas of 4-connected pixel groups for each BWi.

7) Remove all elements from BW_i whose area is more than 3 σBW_i away from μBW_i.

8) Dilate each BW_i with a 3x3 pixel square. If the number of 8-connected pixel groups changes from step 5, go back to step 5. If the number of groups doesn't change, sum all BW_i to produce a new image I_{int}.

9) Apply manual threshold I_{int} to produce a new image I_f. In practice the cut off is usually 7 (corresponding to blocks that have pixel intensities more than μI).

10) Erode I_f with a disk of radius 2.

11) Fill inside 8-connected pixel groups of I_f.

12) Label all 8-connected pixel groups in I_f.

13) Dilate all labeled objects in I_f with a disk of radius 2.

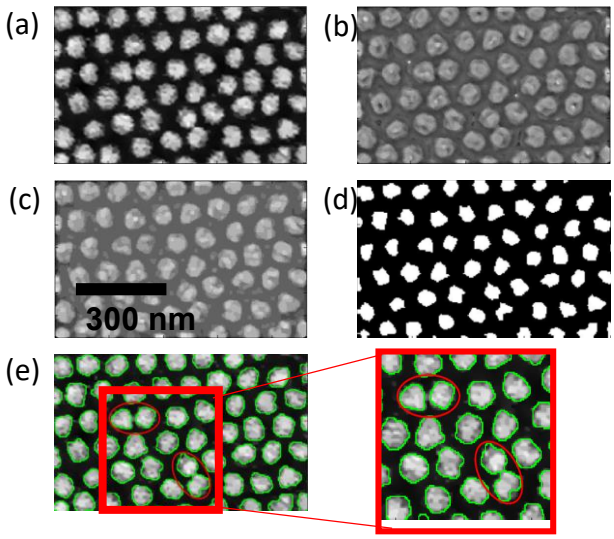

Figure 1.3: (a) Raw SEM image of Ni nanodots on Si substrate produced using AAO template (b) Normalized image (after step 2 in the algorithm) (c) Morphologically filtered image (I_{int} from step 8 in the algorithm) (d) Binary threshold on the morphologically filtered image (after step 9 in the algorithm) (e) Final segmentation (green outlines) superimposed on the raw image. Red ellipses indicate area of minor overlap between nanodots which were nonetheless correctly segmented (f) Zoom in of (e) showing the overlap between dots.

Segmentation is done in two main steps. First, a per-pixel normalization of local intensity (steps 1-2)[50]. Second, an area-based filtering of normalized regions (steps 3-8). Figure 1.3 presents a graphical representation of the segmentation algorithm. The algorithm requires three inputs additional to the raw image. First, whether the regions of

interest are "dark" or "light". Second, the per-pixel normalization length scale (N). Third, the value at which the final threshold (step 9) is performed.

Certain problems, such as segmentation of objects with significant overlap or segmentation of a particular class of ROI in an image with multiple similar sized ROI classes, require a more advanced segmentation capability. This can be achieved by users because the segmentation algorithm is written modularly and can be easily changed/replaced while not affecting other MIST capabilities. Important alternative segmentation methods can be derived from erosion[51], edge detection[52], watershed transformations[53], and machine learning techniques[54].

MIST is used both with built-in and custom user-defined analysis tools. Raw results of the segmentation and of the built-in analysis can be accessed using MATLAB software. Writing additional modules for MIST can also be done in MATLAB. A unique and important feature of MIST is the variety of built-in analysis tools that come with the software (Figure 1.4) that are designed to capture parameters commonly cited in literature on AAO and other self-assembly techniques.

The center-to-center radial two point correlation function (Figure 1.4a) describes the long range order of the ROI. Two useful quantities that can be extracted from the correlation function are the nearest neighbor distance, which is the location of the first peak, and the domain size. We estimate the domain size by considering that the correlation functions consists of oscillations due to lattice properties (which we estimate as the standard deviation of the data in a window of size N) and from small random oscillations which are estimated by fitting a model of Additive White Gaussian Noise

(AWGN)[55]. In particular we define the domain length scale r as the smallest r for which the following is true:

$$\exp\left(-\frac{(\sigma_{r,N}-\sigma_{AWGN})^2}{2\sigma_{AWGN}{}^2}\right)>0.5$$

where $\sigma_{r,N}$ is the standard deviation in the correlation function values around point r in a window of size N (where N is taken to be 150% greater that the first nearest neighbor) and where σ_{AWGN} is the estimate standard deviation of the AWGN over the entire correlation function.

Region of interest average shape (inset into Figure 1.4a) displays anisotropies as well as shape distribution of the ROI. Nearest neighbor angle distribution (Figure 1.4b), together with the radial two-point correlation function, allows comparison to idealized lattice values, which can be used as a "quality" comparison between different samples. Average ROI area (Figure 1.4c), gives information about ROI size, which is one of the most used values extracted from SEM imaging of self-assembled nanostructures. These values, when extracted manually, tend to be biased by human selection towards what is considered "typical". While this bias is not significant for highly uniform arrays of ROIs, when the ROI size distribution is not symmetric human "experts" often select the most common size as the "mean" rather than the true mean. Furthermore, for non-uniform ROIs different human "experts" may use different personal criteria to find the "mean" values thus making comparison across literature difficult. Our algorithm presents a completely automatic way of measuring this value and its uncertainty. Unit cell area distribution (Figure 1.4d) presents information on the uniformity of the lattice. Finally,

the number of nearest neighbors (Figure 1.4e) gives additional information on the "quality" of the lattice.

It is important to note that the ROI at the edges of the image may sometimes bias the statistics. To overcome this MIST counts edge objects whose size is comparable to those of object on the inside and discards those that are too small or too big. The two point correlation function, which is very sensitive to finite size effects, is properly corrected to take into full account the edge effects due to finite image size.

Once the built-in analysis is performed, the raw results together with the per-pixel segmentation data are saved in MATLAB's .mat format. Additional analysis can be applied by loading the .mat file. Most of the parameters needed for these additional analyses, such as ROI labeling, centroid positions, morphological properties, are already computed during the initial segmentation and are readily available

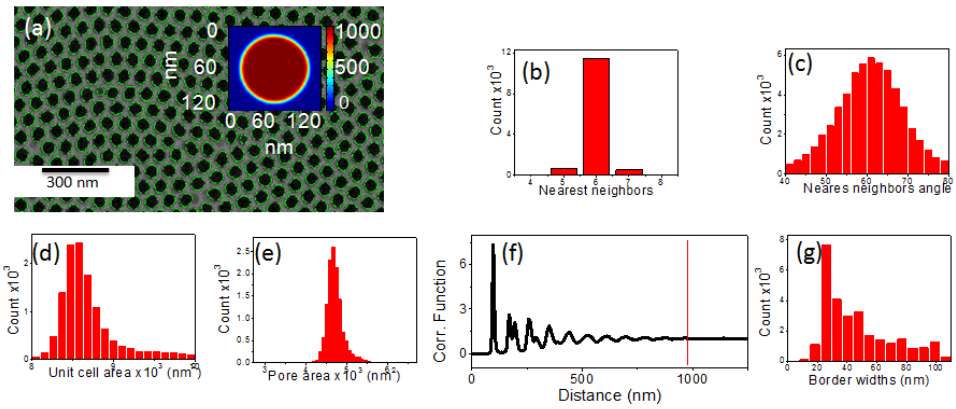

Figure 1.4: Analysis of membrane displayed in (a). Green shows automated segmentation while inset shows average pore shape. (b) Nearest neighbor count (c) nearest neighbor angle distribution (d) unit cell area distribution (e) pore area distribution (g) border width distribution. (f) Radial two-point correlation function. Red line symbolizes the automatically determined length-scale (domain length, 987 nm)

1.4 Acknowledgements

Chapter 1 was in part prepared using a publication: Ilya Valmianski, Carlos Monton, Ivan K. Schuller, " Microscopy Image Segmentation Tool: Robust image data analysis", Review of Scientific Instruments, 85:3 (2014). The dissertation/thesis author was the primary investigator and author of this paper.

1.5 References

1. Imada, M., Fujimori, A. Tokura, Y. Metal-insulator transitions. *Rev. Mod. Phys.* **70,** 1039–1263 (1998).

2. Campi, G., Bianconi, A., Poccia, N., Bianconi, G., Barba, L., Arrighetti, G., Innocenti, D., Karpinski, J., Zhigadlo, N. D., Kazakov, S. M., Burghammer, M., Zimmermann, M. v., Sprung, M., Ricci A., Inhomogeneity of charge-density-wave order and quenched disorder in a high-Tc superconductor. *Nature* **525,** 359–362 (2015).

3. Tokura, Y., Nagosa, N., Orbital physics in transition-metal oxides. *Science* **288,** 462–8 (2000).

4. Ruzmetov, D., Gopalakrishnan, G., Ko, C., Narayanamurti, V. , Ramanathan, S. Three-terminal field effect devices utilizing thin film vanadium oxide as the channel layer. *J. Appl. Phys.* **107,** 114516 (2010).

5. Schmitt, F., Kirchmann, P. S., Bovensiepen, U., Moore, R. G., Rettig, L., Krenz, M., Chu, J.-H., Ru, N., Perfetti, L., Lu, D. H., Wolf, M., Fisher, I. R., Shen, Z.-X., Transient electronic structure and melting of a charge density wave in $TbTe_3$. *Science* **321,** 1649–52 (2008).

6. Basov, D. N., Averitt, R. D., van der Marel, D., Dressel, M. & Haule, K. Electrodynamics of correlated electron materials. *Rev. Mod. Phys.* **83,** 471–541 (2011).

7. Qazilbash, M. M., Schafgans, A. A., Burch, K. S., Yun, S. J., Chae, B. G., Kim, B. J., Kim, H. T., Basov, D. N., Electrodynamics of the vanadium oxides VO_2 and V_2O_3. *Phys. Rev. B* **77,** 115121 (2008).

8. Fausti, D., Tobey, R. I., Dean, N., Kaiser, S., Dienst, A., Hoffmann, M. C., Pyon, S., Takayama, T., Takagi, H., Cavalleri A., Light-induced superconductivity in a stripe-ordered cuprate. *Science* **331,** 189–91 (2011).

9. Ichikawa, H., Nozawa, S., Sato, T., Tomita, A., Ichiyanagi, K., Chollet, M.,

Guerin, L., Dean, N., Cavalleri, A., Adachi, S., Arima, T., Sawa, H., Ogimoto, Y., Nakamura, M., Tamaki, R., Miyano, K., Koshihara, S., Transient photoinduced 'hidden' phase in a manganite. *Nat. Mater.* **10,** 101–5 (2011).

10. Fratini, M., Poccia, N., Ricci, A., Campi, G., Burghammer, M., Aeppli, G., Bianconi, A., Scale-free structural organization of oxygen interstitials in La_2CuO_{4+y}. *Nature* **466,** 841–844 (2010).

11. Porer,M., Leierseder, U., Ménard, J.-M., Dachraoui, H., Mouchliadis, L., Perakis, I. E., Heinzmann, U., Demsar, J., Rossnagel, K., Huber, R., Non-thermal separation of electronic and structural orders in a persisting charge density wave. *Nat. Mater.* **13,** 857–61 (2014).

12. Dernier, P. D. & Marezio, M. Crystal structure of the low-temperature antiferromagnetic phase of V_2O_3. *Phys. Rev. B* **2,** 3771–3776 (1970).

13. Carter, S. A., Rosenbaum, T. F., Lu, M., Jaeger, H.M., Metcalf, P., Honig, J.M., Spalek, J., Magnetic and transport studies of pure V_2O_3 under pressure. *Phys. Rev. B* **49,** 7898–7903 (1994).

14. Balents, L. Spin liquids in frustrated magnets. *Nature* **464,** 199–208 (2010).

15. Kyung, B. & Tremblay, A.-M. S. Mott transition, antiferromagnetism, and d-wave superconductivity in two-dimensional organic conductors. *Phys. Rev. Lett.* **97,** 46402 (2006).

16. Bednorz, J. G. & Müller, K. A. Possible high T_c superconductivity in the Ba−La−Cu−O system. *Zeitschrift für Phys. B Condens. Matter* **64,** 189–193 (1986).

17. Wu, M. K., Ashburn, J. R., Torng, C. J., Hor, P. H., Meng, R. L., Gao, L., Huang, Z. J., Wang, Y. Q., Chu,C. W., Superconductivity at 93 K in a new mixed-phase Y-Ba-Cu-O compound system at ambient pressure. *Phys. Rev. Lett.* **58,** 908–910 (1987).

18. Jin, S., Tiefel, T. H., McCormack, M., Fastnacht, R. A., Ramesh, R., Chen, L. H., Thousandfold change in resistivity in magnetoresistive La-Ca-Mn-O films. *Science (80).* **264,** 413 LP-415 (1994).

19. Haldane, F. D. M. Nonlinear field theory of large-spin heisenberg antiferromagnets: Semiclassically quantized solitons of the one-dimensional easy-axis Néel state. *Phys. Rev. Lett.* **50,** 1153–1156 (1983).

20. Laughlin, R. B. Quantized Hall conductivity in two dimensions. *Phys. Rev. B* **23,** 5632–5633 (1981).

21. Hasan, M. Z. & Kane, C. L. Colloquium: Topological insulators. *Rev. Mod. Phys.*

82, 3045–3067 (2010).

22. Helton, J.S., Matan, K., Shores, M.P., Nytko, E.A., Bartlett, B.M., Yoshida, Y., Takano, Y., Suslov, A., Qiu, Y., Chung, J.-H., Nocera, D.G., Lee, Y.S., Spin dynamics of the spin-1/2 Kagome lattice antiferromagnet $ZnCu_3(OH)\ Cl_2$. *Phys. Rev. Lett.* **98,** 107204 (2007).

23. McWhan, D. B., Menth, A., Remeika, J. P., Brinkman, W. F. & Rice, T. M. Metal-insulator transitions in pure and doped V_2O_3. *Phys. Rev. B* **7,** 1920–1931 (1973).

24. Mott, N. F. The basis of the electron theory of metals, with special reference to the transition metals. *Proc. Phys. Soc. Sect. A* **62,** 416 (1949).

25. Rühle, S., Anderson, A. Y., Barad, H.-N., Kupfer, B., Bouhadana, Y., Rosh-Hodesh, E., Zaban, A., All-oxide photovoltaics. *J. Phys. Chem. Lett.* **3,** 3755–3764 (2012).

26. Elumalai, N. K., Vijila, C., Jose, R., Uddin, A. & Ramakrishna, S. Metal oxide semiconducting interfacial layers for photovoltaic and photocatalytic applications. *Mater. Renew. Sustain. Energy* **4,** 11 (2015).

27. Linsebigler, A. L., Lu, G. & Yates, J. T. Photocatalysis on TiO_2 surfaces: Principles, mechanisms, and selected results. *Chem. Rev.* **95,** 735–758 (1995).

28. Djurisic, A. B., Leung, Y. H. & Ching Ng, A. M. Strategies for improving the efficiency of semiconductor metal oxide photocatalysis. *Mater. Horiz.* **1,** 400–410 (2014).

29. Burchhart, T., Lugstein, A., Hyun, Y. J., Hochleitner, G. & Bertagnolli, E. Atomic Scale Alignment of copper-germanide contacts for Ge nanowire metal oxide field effect transistors. *Nano Lett.* **9,** 3739–3742 (2009).

30. Argall, F. Switching phenomena in titanium oxide thin films. *Solid. State. Electron.* **11,** 535–541 (1968).

31. Beck, A., Bednorz, J. G., Gerber, C., Rossel, C. & Widmer, D. Reproducible switching effect in thin oxide films for memory applications. *Appl. Phys. Lett.* **77,** 139–141 (2000).

32. Snider, G., Amerson, R., Carter, D., Abdalla, H., Qureshi, M. S., Leveille, J., Versace, M., Ames, H., Patrick, S., Chandler, B., Gorchetchnikov, A., Mingolla, E., From synapses to circuitry: Using memristive memory to explore the electronic brain. *Computer (Long. Beach. Calif).* **44,** 21–28 (2011).

33. Ladd, T. D., Jelezko, F., Laflamme, R., Nakamura, Y., Monroe, C., O'Brien, J. L., Quantum computers. *Nature* **464,** 45–53 (2010).

34. McWhan, D. B., Remeika, J. P., Rice, T. M., Brinkman, W. F., Maita, J. P., Menth, A., Electronic specific heat of metallic Ti-doped V_2O_3. *Phys. Rev. Lett.* **27,** 941–943 (1971).

35. Sass, B., Tusche, C., Felsch, W., Quaas, N., Weismann, A., Wenderoth, M., Structural and electronic properties of epitaxial V_2O_3 thin films. *J. Phys. Condens. Matter* **16,** 77 (2004).

36. Schwingenschlgl, U. & Eyert, V. The vanadium Magneli phases V_nO_{2n-1}. *Ann. der Phys.* **13,** 475–510 (2004).

37. Biermann, S., Poteryaev, A., Lichtenstein, A. I. & Georges, A. Dynamical singlets and correlation-assisted peierls transition in VO_2. *Phys. Rev. Lett.* **94,** (2005).

38. Tanaka, A. Electronic Structure and Phase Transition in V_2O_3: Importance of 3d spin-orbit interaction and lattice distortion. *J. Phys. Soc. Japan* **71,** 1091–1107 (2002).

39. Hansmann, P., Toschi, A., Sangiovanni, G., Saha-Dasgupta, T., Lupi, S., Marsi, M., Held, K., Mott-Hubbard transition in V_2O_3 revisited. *Phys. status solidi* **250,** 1251–1264 (2013).

40. Misochko, O. V., Tani, M., Sakai, K., Kisoda, K., Nakashima, S., Andreev, V. N., Chudnovsky, F. A., Optical study of the Mott transition in V_2O_3. *Phys. Rev. B* **58,** 12789–12794 (1998).

41. Saerbeck, T., Venta, J., Wang, S., Ramírez, J. G., Erekhinsky, M., Valmianski, I., Schuller, I. K., Coupling of magnetism and structural phase transitions by interfacial strain. *J. Mater. Res.* **29,** 2353–2365 (2014).

42. Brockman, J., Samant, M. G., Roche, K. P. & Parkin, S. S. P. Substrate-induced disorder in V_2O_3 thin films grown on annealed c-plane sapphire substrates. *Appl. Phys. Lett.* **101,** 51606 (2012).

43. McWhan, D. B. & Remeika, J. P. Metal-insulator transition in $(V_{1-x}Cr_x)_2O_3$. *Phys. Rev. B* **2,** 3734–3750 (1970).

44. Limelette, P., Georges, A., Jérome, D., Wzietek, P., Metcalf, P., Honig, J. M., Universality and critical behavior at the Mott transition. *Science (80).* **302,** 89–92 (2003).

45. McLeod, A. S., Heumen, E. van, Ramirez, J. G., Wang, S., Saerbeck, T., Guenon, S., Goldflam, M., Anderegg, L., Kelly, P., Mueller, A., Liu, M. K., Schuller, I.K., Basov, D. N., Nanotextured phase coexistence in the correlated insulator V_2O_3. *Nat. Phys.* (2016). doi:10.1038/nphys3882

46. Guénon, S., Scharinger, S., Wang, S., Ramírez, J.G., Koelle, D., Kleiner, R.,

Schuller, I.K., Electrical breakdown in a V_2O_3 device at the insulator-to-metal transition. *Europhys. Lett.* **101,** 57003 (2013).

47. Ramirez, J. G., Saerbeck, T., Wang, S., Trastoy, J., Malnou, M., Lesueur, J., Crocombette, J.-P., Villegas, J. E., Schuller, I. K., Effect of disorder on the metal-insulator transition of vanadium oxides: Local versus global effects. *Phys. Rev. B* **91,** 205123 (2015).

48. Wang, S., Ramirez, J. G. & Schuller, I. K. Avalanches in vanadium sesquioxide nanodevices. *Phys. Rev. B - Condens. Matter Mater. Phys.* **92,** (2015).

49. Pennycook, S.J., Zhouc, H., Chisholma, M.F., Borisevicha, A.Y., Varelaa, M., Gazquezd, J., Pennycook, T.J., Narayan, J., Misfit accommodation in oxide thin film heterostructures. *Acta Mater.* **61,** 2725–2733 (2013).

50. Valmianski, I., Shih, A.Y., Driscoll, J.D., Matthews, D.W., Freund, Y., Kleinfeld, D., Automatic identification of fluorescently labeled brain cells for rapid functional imaging. *J. Neurophysiol.* **104,** 1803–11 (2010).

51. Anoraganingrum, D. Cell segmentation with median filter and mathematical morphology operation. in *Proceedings 10th International Conference on Image Analysis and Processing* 1043–1046 (1999). doi:10.1109/ICIAP.1999.797734

52. Perona, P. & Malik, J. Scale-space and edge detection using anisotropic diffusion. *IEEE Trans. Pattern Anal. Mach. Intell.* **12,** 629–639 (1990).

53. Shafarenko, L., Petrou, M. & Kittler, J. Automatic watershed segmentation of randomly textured color images. *IEEE Trans. Image Process.* **6,** 1530–1544 (1997).

54. Ren, X. & Malik, J. Learning a classification model for segmentation. in *Proceedings Ninth IEEE International Conference on Computer Vision* 10–17 vol.1 (2003). doi:10.1109/ICCV.2003.1238308

55. Hughes, B. On the error probability of signals in additive white Gaussian noise. *IEEE Trans. Inf. Theory* **37,** 151–155 (1991).

Chapter 2 - Photoinduced pathway to a metastable phase in V_2O_3

In quantum materials, subtle changes in atomic-scale interactions induce dramatic changes in macroscopic materials properties and drive phase transitions[1,2]. Despite their importance[3–6], the mesoscale processes underpinning phase transitions in time and space often remain elusive because of the vast differences in time scales between atomic and electronic changes and thermodynamic transformations. Here, we photo excite an ultrafast enhancement of the structural mesoscale long-range order in the archetypal Mott system V_2O_3. The rearrangement of local atomic distances is much slower and coincides with the insulator-to-metal transition[7]. The decoupling between the two structural responses in time reveal the existence of a transient photoinduced phase, which is distinct from the two structural phases present in equilibrium. X-ray nanoscopy reveals that acoustic phonons trapped in nanoscale blocks govern the dynamics of the ultrafast transition into the photoinduced phase, while nucleation and growth of metallic domains dictate the duration of the slower transition into the metallic phase[7]. The presence of mesoscale structural rearrangements before completion of the electronic transition, emphasize the critical role of metastable intermediate sructural phases in electronic phase transitions.

Vanadium sesquioxide (V_2O_3) undergoes an insulator-to-metal transition upon heating at 160 K: the electric conductivity grows by five orders of magnitude via percolation of the high-temperature (HT) paramagnetic, metallic domains within the low-temperature (LT) antiferromagnetic, insulating domains [8–10]. The electronic phase transition is accompanied by a structural phase transition, where the crystal symmetry increases from monoclinic to rhombohedral, and the volume shrinks via reduction of the

average hexagon edge from 2.91 Å to 2.87 Å (see Fig. 2.1**a**)[11–13]. While the symmetry and volume are coupled in equilibrium, here we show that ultrafast photoexcitation decouples these structural degrees of freedom, and the phase transformation occurs via a non-equilibrium transient pathway (see Fig. 2.1**b**).

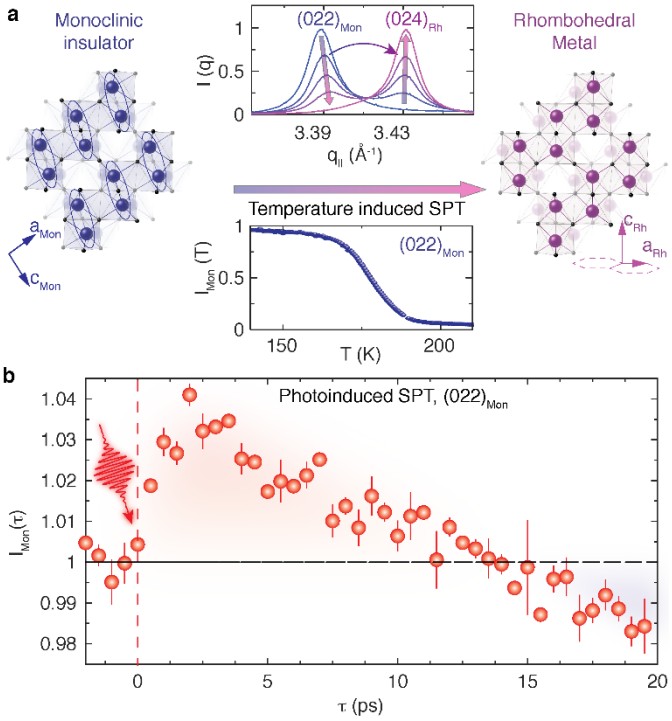

Figure 2.1: Temperature and photo induced structural phase transition. a, A schematic of the equilibrium insulating (monoclinic, rotation of vanadium pairs is indicated by ellipses) and metallic (rhombohedral) structure. The transition occurs directly during heating evidenced by a smooth reduction of the $(022)_{Mon}$ monoclinic and growth of the $(024)_{Rh}$ rhombohedral peak (see inset). **b** The peak intensity of the $(022)_{Mon}$ reflection as a function of the time delay during the photoexcited structural phase transition.

We study a 100 nm thin V_2O_3 film grown along the $(024)_{Rh}$ crystallographic direction (see Supplement). The difference in the hexagon edge lengths results in two well separated X-ray Bragg peaks along the film normal, $q_\perp$: $(024)_{Rh}$ and $(022)_{Mon}$ (see inset in Fig. 2.1**c**). The LT diffraction peak is broader than the HT peak in the direction

parallel to the film, $q_{\parallel}$ (see inset in Fig. 2.1**c**). The excess broadening results from a reduction of the long-range order (coherence length) due to breaking of the crystal symmetry at low temperatures. Three monoclinic structures are possible, each distorted along a different hexagon edge[11,12]. When heated in equilibrium through the phase transition temperature, the height of the HT peak grows, while the height of the LT peak decreases monotonically. The LT diffraction peak width is proportional to the LT peak height, while the width of the HT peak is static.

We use short, optical laser pulses (E=1.55 eV, 40 fs duration, 500 μm spot size) to induce an insulator-to-metal phase transition in V_2O_3. We probe the structural response to photoexcitation with short x-ray pulses (E = 9 keV, 10 fs duration, 200 μm spot size) in stroboscopic mode at the Linac Coherent Light Source[14,15]. After photoexcitation, the height of the HT peak grows as expected (see Fig. 2.1**c**) as the optical laser pulse heats the film. Because the HT peak grows, one may expect a drop in the LT peak height. Unexpectedly, the height of the LT peak grows for 2.5 ps before it declines for larger time delays (see Fig. 2.1**d**). From the 4D data set (3D reciprocal space and time, see Supplement Fig. S3), we find that the LT peak height grows by narrowing the LT peak. Since the peak broadening in the ground state originates from the decrease in long range order, we conclude that photoexcitation induces higher symmetry in the LT phase after 2.5 ps. At these short timescales however, the photoexcited LT phase retains its unit cell volume, as revealed by the unmodified Bragg peak position (see Fig. 2.1**b**). Thus, photoexcitation induces a transient, non-equilibrium, structural phase in V_2O_3.

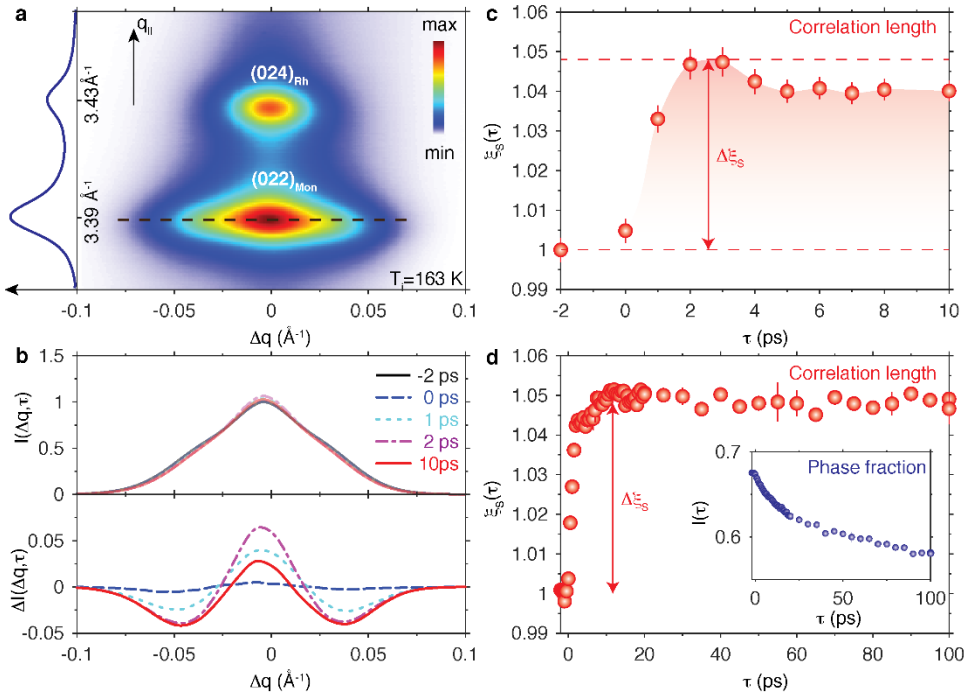

Figure 2.2. Time resolved high-resolution x-ray data. a, A projection of the 3D diffraction data around the $(022)_{Mon}$ and $(024)_{Rh}$ Bragg peaks recorded for a negative time delay (ground state) shown on a linear scale. **b,** A line scan $I(\Delta q,\tau)$ normalized by its maximum along the black dashed line in **a** for various time delays and the difference signal $I(\Delta q, \tau)$-$I_0(\Delta q)$, where $I_0=I(\Delta q,\tau=-2$ ps). **c,d** The correlation length $\xi(\tau)$ calculated as the reciprocal peak width in **b** (see Methods). Inset in **d**, Phase fraction of the monoclinic phase.

The photoinduced structural phase transition displays two processes with vastly different characteristic time scales. First, the structural coherence length in the photoexcited LT phase, $\xi(\tau)$, grows rapidly within 2.5 ps (see Fig 2.2**a**, left axis) and remains high for more than 100 ps. Second, the HT phase fraction, $V_{HT}(\tau)$, grows gradually within 100 ps after photoexcitation, and the unit cell volume of the photoexcited LT phase shrinks discontinuously and the HT phase emerges (see Fig. 2.2**a**, right axis). Furthermore, the coherence length and the phase fraction depend differently on the pump fluence. The coherence length ξ(2.5ps) increases linearly with the pump fluence before it saturates at ~5 mJ/cm^2 (see Fig. 2.2**b**). The saturation value at 1.3 agrees

with the maximum coherence length of the LT phase measured in equilibrium. In contrast, the final HT phase fraction V_{HT}(100 ps) displays a fluence threshold[7,16] at around 1 mJ/cm^2: the growth rate increases significantly when the pump energy overcomes the energy barrier due to the latent heat (see Fig. 2,2**c**). At fluences higher than 5 mJ/cm^2 the phase fraction V_{HT}(100 ps) saturates at its maximum value of one, when the entire volume is in the HT phase. While the presence of the fluence threshold and the duration of the HT phase growth are both consistent with the photoinduced electronic transition[7], the origin of the 2.5 ps time scale remains elusive. To understand the mechanism underpinning this ultrafast coherence length growth, we use X-ray nanoscopy.

We map the static nanoscale spatial distribution of the two structural phases by scanning a 20 nm X-ray beam across the sample (see Fig. 2.3**a**). The typical size of an LT domain (connected blue region in Fig. 2.3**a**) is 100 nm, consistent with near-field imaging of insulating and metallic pockets[10]. Surprisingly, the broadening of the LT diffraction peak is present in the diffraction collected during a single exposure by the 20 nm nanobeam (see Fig. 2.3**b**). Thus, structural disorder is induced on a much smaller length scale than the size of a LT domain. X-ray diffraction at higher angles reveals splitting of the LT phase into a mosaic of two distinct types of crystallites angularly misaligned to each other by 1° about the film normal. The two categories correspond to monoclinic distortions either along the A or B directions (Figs. 2.3**c**). Statistical analysis (see Supplement and Fig. S6) of 20,000 diffraction patterns collected while scanning the nanobeam across the film yields an average crystallite size of ξ = 8 nm (Fig. 2.3**c**). The spatially resolved peak broadening is homogeneous and independent of the LT peak

intensity, suggesting a random distribution of the crystallites throughout the film. The diffraction peak corresponding to the monoclinic distortion along the third direction appears at a different momentum transfer[11] and is only noticeable at the lowest temperatures.

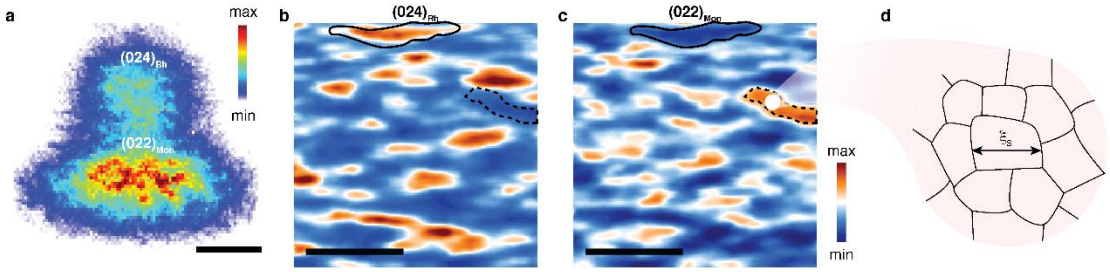

Figure 2.3. Nanoscale mapping of the lattice distortion. **a** Typical diffraction signal recorded with the nanobeam. **b,c** The phase distribution revealed by intensity of the $(022)_{Mon}$ (**b**) and $(024)_{Rh}$ (**c**) peaks recorded by scanning the nanobeam. The areas marked with solid (dashed) lines represent rhombohedral (monoclinic) pockets. **d** A schematic of the distribution of an insulating pocket into mutually misaligned domains. Scale bar is 0.04 $Å^{-1}$ in **a**, and 1 μm in **b**,**c**.

The combination of time-resolved diffraction and x-ray nanoscopy implies that the photoexcited structural phase transition proceeds as follows (Fig. 2.3**d**): Photoexcitation enhances the coherence length through a collective alignment of the crystallites within 2.5 ps. This ultrafast time scale (Fig. 2.1**d**) is in agreement with the half period $\tau_P/2 = L/v$ of the coherent phonon at the Brillouin zone boundary[17], where L= 8 nm is the size of the crystallite and $v = 2.5$ nm/ps is the sound velocity in monoclinic V_2O_3 (Ref. [18]). The 8 nm large crystallites act as internal traps for acoustic phonons, which drive the symmetry enhancement by shear motion[19]. The degree of alignment grows linearly with pump fluence (Fig. 2.2**b**), characteristic of a second-order phase transition as described by Landau-Ginzburg theory extended to ultrafast

transitions[20]. The photoinduced phase transition completes with a unit cell volume contraction within 100 ps, while the crystallites remain aligned with an enhanced coherence length.

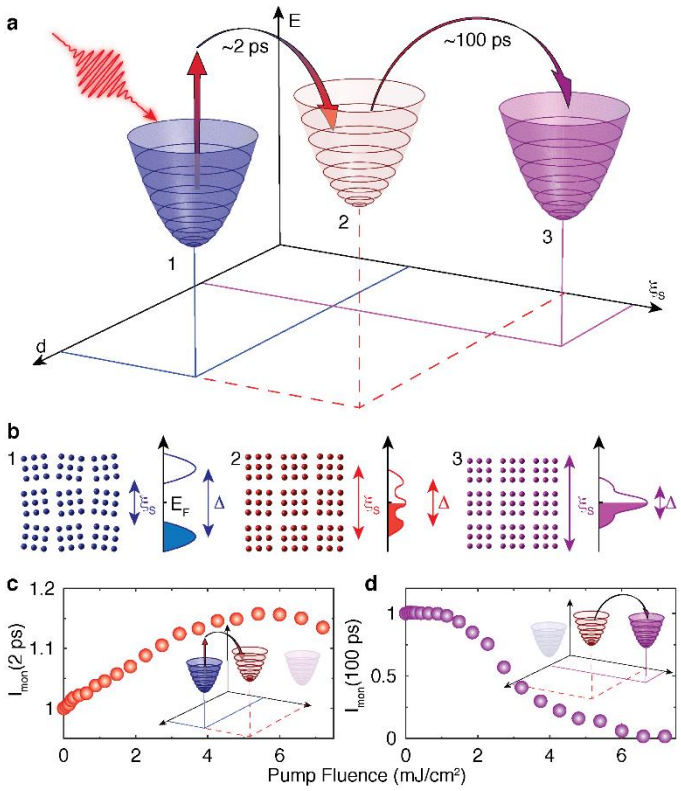

Figure 2.4: The dynamic structural phase transition. a Dynamically evolving potential energy surface during the photoinduced insulator to metal transition**.** The transition occurs in two steps: increase of the in plane correlation length in 2 ps followed by the discontinuous out of plane lattice parameter, d, change in 100 ps. **b** Schematic evolution of the structure and the electronic properties during the SPT. 1: In the low temperature ground state the domains are misaligned and the electronic system is gapped. 2: Photoexcitation induces an enhancement of the correlation length (collective alignment of the domains) and a partial closing of the gap. 3: The lattice parameter changes discontinuously, the Mott gap closes and the equilibrium metallic state is established. **c** The peak intensity of the monoclinic reflection after 2 ps and 100 ps as a function of pump fluence representing the ultrafast correlation length enhancement and the phase fraction after completion of the SPT, respectively.

This longer process displays a fluence threshold arising from the latent heat and is the hallmark of a first-order phase transition[7,16]. The volume contraction is governed by

the nucleation and ballistic growth through 100 nm large LT domains moving at the sound velocity [7] (see Fig. 2.3**a**).

Laser pulse energies well below the fluence threshold align the crystallites in the LT phase, yet avoid the transition into the HT phase. At these low fluences the enhanced long-range order prevails for more than 100 ps as measured in our experiment. This duration represents the lower time scale for the spontaneous symmetry breaking into structurally equivalent monoclinic lattices, whose presence possibly stabilizes the transient higher symmetry phase. Above the fluence threshold the coherence length enhancement and the HT phase fraction growth both saturate at 5 mJ/cm^2, indicating that the transient non-equilibrium state is a precursor to the metallic state.

The size of the monoclinic crystallites ξ we determine from X-ray nanoscopy is in excellent agreement with the electronic correlation length ξ_{el} found in bulk V_2O_3 (Ref. [21]). We conclude a strong interdependence between the electronic correlations and structural twinning of the LT phase into different monoclinic crystallites in equilibrium. By assuming that the electronic correlation length and the crystallite size remain coupled after photoexcitation $\xi_{el}(\tau)=\xi(\tau)$ we estimate the dynamic Mott gap via $\Delta(\tau)\sim 1/\xi(\tau)^2$ (Refs.[1,21]). The photoexcitation induces an ultrafast alignment of the crystallites, which effectively increases the coherence length and induces a narrowing of the band gap (Fig. 2.3**d**). The maximum dynamic correlation length in the monoclinic phase is smaller than the correlation length in the rhombohedral phase; thus the gap is not closed entirely, consistent with the existence of a dynamic pseudogap observed in other Mott systems[22].

The photoexcited phase is similar to the paramagnetic insulating phase, which in equilibrium occurs with chromium doping or equivalently with negative pressure[11–13].

Thus, the observation of the ultrafast quench of the monoclinic distortion indicates an ultrafast quench of the antiferromagnetic order. This is further supported by the negative thermal expansion in V_2O_3 within the a-b plane, which results in transient negative pressure after photoexcitation. In addition, the photoinduced insulator-to-metal transition in V_2O_3 lasts for tens of picoseconds, consistent with the duration of the structural volume change reported here. The long-range order enhancement through cooperative nanoscale alignment completes earlier. Because long-range order is essential for electronic transport[8], we anticipate that the presence of the photoinduced structural order impacts the dynamics of the electronic transition, a behavior which is incompatible with the standard description of a Mott system.

Acknowledgements

Chapter 2 was prepared based on a paper that is to be submitted with the following author list: Andrej Singer, Juan Gabriel Ramirez, Ilya Valmianski, Devin Cela, Nelson Hua, Roopali Kukreja, James Wingert, Olesya Kovalchuk, James M. Glownia, Marcin Sikiroski, Matthieu Chollet, Martin Holt, Ivan K. Schuller, and Oleg G. Shpyrko. A.S and J.G.R. conceived of the idea. A.S., J.G.R., I.K.S., and O.G.S planned the experiment. J.G.R. and I.V. prepared the samples and performed resistance measurements for in-situ calibration. A.S, J.G.R, I.V., D.C, N.H., R.K., O.K., J.M.G., M.S., M.Ch., and O.G.S. conducted the time resolved experiment. A.S., N.H., J.W., and M.H. conducted the nanodiffraction experiment. A.S. analyzed the data. All authors discussed the interpretation of the data. A.S., J.G.R., and I.V. wrote the paper with input from all authors. The dissertation/thesis author was a major contributor to this paper.

References

1. Imada, M., Fujimori, A. & Tokura, Y. Metal-insulator transitions. *Rev. Mod. Phys.* **70,** 1039–1263 (1998).

2. Dagotto, E. Complexity in strongly correlated electronic systems. *Science* **309,** 257–62 (2005).

3. Fratini, M., Poccia, N., Ricci, A., Campi, G., Burghammer, M., Aeppli, G. & Bianconi, A. Scale-free structural organization of oxygen interstitials in La_2CuO_{4+y}. *Nature* **466,** 841–844 (2010).

4. Kohsaka, Y., Hanaguri, T., Azuma, M., Takano, M., Davis, J. C. & Takagi, H. Visualization of the emergence of the pseudogap state and the evolution to superconductivity in a lightly hole-doped Mott insulator. *Nat. Phys.* **8,** 534–538 (2012).

5. Zeljkovic, I., Xu, Z., Wen, J., Gu, G., Markiewicz, R. S. & Hoffman, J. E. Imaging the Impact of Single Oxygen Atoms on Superconducting $Bi_{2+y}Sr_{2-y}CaCu_2O_{8+x}$. *Science (80-.).* **337,** 320–323 (2012).

6. Campi, G., Bianconi, A., Poccia, N., Bianconi, G., Barba, L., Arrighetti, G., Innocenti, D., Karpinski, J., Zhigadlo, N. D., Kazakov, S. M., Burghammer, M., Zimmermann, M. v., Sprung, M. & Ricci, A. Inhomogeneity of charge-density-wave order and quenched disorder in a high-Tc superconductor. *Nature* **525,** 359–362 (2015).

7. Abreu, E., Wang, S., Ramírez, J. G., Liu, M., Zhang, J., Geng, K., Schuller, I. K. & Averitt, R. D. Dynamic conductivity scaling in photoexcited V_2O_3 thin films. *Phys. Rev. B* **92,** 85130 (2015).

8. Ramirez, J. G., Saerbeck, T., Wang, S., Trastoy, J., Malnou, M., Lesueur, J., Crocombette, J.-P., Villegas, J. E. & Schuller, I. K. Effect of disorder on the metal-insulator transition of vanadium oxides: Local versus global effects. *Phys. Rev. B* **91,** 205123 (2015).

9. De La Venta, J., Wang, S., Saerbeck, T., Ramírez, J. G., Valmianski, I. & Schuller, I. K. Coercivity enhancement in V_2O_3/Ni bilayers driven by nanoscale phase coexistence. *Appl. Phys. Lett.* **104,** (2014).

10. McLeod, A. S., van Heumen, E., Ramirez, J. G., Wang, S., Saerbeck, T., Guenon, S., Goldflam, M., Anderegg, L., Kelly, P., Mueller, A., Liu, M. K., Schuller, I. K. & Basov, D. N. Nanotextured phase coexistence in the correlated insulator V2O3. *Nat. Phys.* (2016).

11. Dernier, P. D. & Marezio, M. Crystal Structure of the Low-Temperature

Antiferromagnetic Phase of V_2O_3. *Phys. Rev. B* **2,** 3771–3776 (1970).

12. McWhan, D. B. & Remeika, J. P. Metal-Insulator Transition in $(V_{1-x}Cr_x)_2O_3$. *Phys. Rev. B* **2,** 3734–3750 (1970).

13. McWhan, D. B., Menth, A., Remeika, J. P., Brinkman, W. F. & Rice, T. M. Metal-insulator transitions in pure and doped V2O3. *Phys. Rev. B* **7,** 1920–1931 (1973).

14. Emma, P., Akre, R., Arthur, J., Bionta, R., Bostedt, C., Bozek, J., Brachmann, A., Bucksbaum, P., Coffee, R., Decker, F.-J., Ding, Y., Dowell, D., Edstrom, S., Fisher, A., Frisch, J., Gilevich, S., Hastings, J., Hays, G., HeringPh., First lasing and operation of an angstrom-wavelength free-electron laser. *Nat Phot.* **4,** 641–647 (2010).

15. Zhu, D., Feng, Y., Stoupin, S., Terentyev, S. A., Lemke, H. T., Fritz, D. M., Chollet, M., Glownia, J. M., Alonso-Mori, R., Sikorski, M., Song, S., van Driel, T. B., Williams, G. J., Messerschmidt, M., Boutet, S., Blank, V. D., Shvyd'ko, Y. V & Robert, A. Performance of a beam-multiplexing diamond crystal monochromator at the Linac Coherent Light Source. *Rev. Sci. Instrum.* **85,** 63106 (2014).

16. Pashkin, A., Kübler, C., Ehrke, H., Lopez, R., Halabica, A., Haglund, R. F., Huber, R. & Leitenstorfer, A. Ultrafast insulator-metal phase transition in VO_2 studied by multiterahertz spectroscopy. *Phys. Rev. B* **83,** 195120 (2011).

17. Park, H., Wang, X., Nie, S., Clinite, R. & Cao, J. Mechanism of coherent acoustic phonon generation under nonequilibrium conditions. *Phys. Rev. B* **72,** 100301 (2005).

18. Elsa, A., Stephanie N. Gilbert Corder, Sun Jin Yun, S. W., Ramirez, J. G., West, K., Zhang, J., Kittiwatanakul, S., Schuller, I. K., Lu, J., Wolf, S. A., Kim, H.-T., Liu, M. & Averitt, R. D. Ultrafast Electron-Lattice Coupling Dynamics in VO_2 and V_2O_3 Thin Films. *arXiv* 1701.05531 (2017).

19. Baum, P., Yang, D.-S. & Zewail, A. H. 4D Visualization of Transitional Structures in Phase Transformations by Electron Diffraction. *Science (80).* **318,** 788–792 (2007).

20. Beaud, P., Caviezel, A., Mariager, S. O., Rettig, L., Ingold, G., Dornes, C., Huang, S.-W., Johnson, J. A., Radovic, M., Huber, T., Kubacka, T., Ferrer, A., Lemke, H. T., Chollet, M., Zhu, D., Glownia, J. M., Sikorski, M., Robert, A., Wadati, H., A time-dependent order parameter for ultrafast photoinduced phase transitions. *Nat. Mater.* **13,** 923–7 (2014).

21. Limelette, P., Georges, A., Jerome, D., Wzietek, P., Metcalf, P. & Honig, J. M. Universality and Critical Behavior at the Mott Transition. *Science (80).* **302,** 89–

92 (2003).

22. Sohrt, C., Stange, A., Bauer, M. & Rossnagel, K. How fast can a Peierls-Mott insulator be melted? *Faraday Discuss.* **171,** 243–57 (2014).

Chapter 3 – Electrically driven breakdown in vanadium oxide nanodevices

Metal to insulator phase transition (MIT) materials are highly sensitive to small perturbations, generating strong electrical[1–6], optical[7–9], or magnetic responses[10–13]. For device applications, it is therefore important to control this change with either current or voltage. While current driven MITs have been shown in several systems, there is an open question of whether the effect is thermally or electric field driven, which is critical for tuning new device applications[1,6]. In this paper, we experimentally study current driven transitions in nanodevices of two important MIT materials, vanadium dioxide (VO_2) and vanadium sesquioxide (V_2O_3). We find that neither simple electric field nor purely thermal models can explain the nanodevice's behavior. However, quantitative agreement can be achieved using a highly heterogeneous thermoelectric model, which we implement using a finite-element approach. The MIT occurs through a surface confined filament, which is determined by the competition between Joule heating, thermal dissipation, and local electric field. These highly confined filaments have very large thermal gradients generating large Seebeck electric fields. Therefore, the physics of the MITs in VO_2 and V_2O_3 in nanodevices is driven by the competing length scales in the filament, which also generate large electric fields normal to the driving field.

VO_2 and V_2O_3 share many phenomenological characteristics; however, there is a debate about the physical origins of their MITs[14–18]. Canonically, in V_2O_3, the MIT is a Mott transition[14,15] with a Slater-like antiferromagnetic ordering[16,17], while, in VO_2, there is dimerization due to a Peierls transition, with some on-site repulsion and no change in magnetism[18]. Both materials have a highly percolative transition resulting in a large region of coexistence of both metallic and insulating domains[14,19,20].

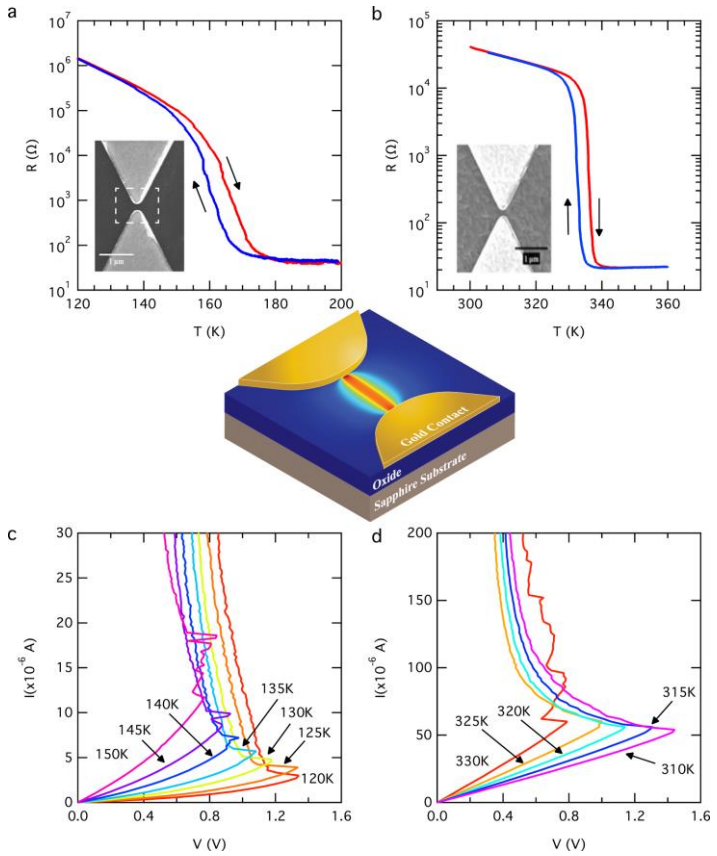

Figure 3.1: (a) Resistivity-temperature characteristic of a typical VO_2 device (SEM image in the inset, light is metallic electrode, dark is VO_2). Blue line signifies the cooling branch, while the red line signifies the heating branch. (b) Resistivity-temperature characteristic of a typical V_2O_3 device. Blue and red lines signify cooling and heating branches respectively. I-V characteristics of the (c) V_2O_3 and (d) VO_2 devices. Temperatures specify the base temperatures of the devices. Middle inset is 3D rendering of a device with a simulated current density in between the electrodes.

We fabricated VO_2 and V_2O_3 nanodevices in the same geometry (see inset Fig 1a) and performed measurements of the IV characteristic through the MIT breakdown as a function of base temperature. Resistivity dependence on temperature in both types of devices is shown in Fig. 3.1a,c. Both devices show three and a half order of magnitude change in resistance with temperature. VO_2 transition temperatures were 332 K and 336 K for the cooling and heating branches respectively, similar to bulk[16], while the V_2O_3

transition temperatures were slightly elevated at 160 K and 166 K[21]. The R-T curves are reproducible and very sensitive to the temperature of the filament. This property allows us to use the resistance of the device before the MIT, when the current and temperature distributions are still mostly homogenous, as a measure of local temperature[1].

Current-voltage characteristic (IV curves) for various starting temperatures are shown on Fig. 1b for V_2O_3 and on Fig. 1d for VO_2. They are obtained by slowly (1 μA/s) ramping up the current while keeping the substrate at a fixed temperature. A region of negative differential resistance corresponds to a current induced MIT. While the IV curve is smooth before the transition, it undergoes multiple jumps as the device goes through the MIT due to an avalanche-like behavior[20]. The initial large jump is due to the filament percolating through the entire device[5]. We obtain the change in the temperature of the device below MIT as a function of dissipated power (Fig. 3.2a, b) by extracting the temperature from the R-T curves (Fig. 3.1) and computing the dissipated power as the IV product. VO_2 (Fig. 3.2a) shows a linear relationship between dissipated power and change in temperature, with lower base temperatures requiring higher dissipated power. This is consistent with previous studies in microscopic VO_2 devices[1] and also a simple Fourier Law based model. However, in V_2O_3 (Fig. 3.2b) the temperature changes sublinearly as a function of power dissipated and, surprisingly, the dissipated power needed to induce MIT does not increase with lower base temperatures. In Fig. 3.2c we compare the effective breakdown electric field with the square root of the breakdown fluence in an optical V_2O_3 experiment[22]. The two curve agree up to a scaling factor, which suggests that while the V_2O_3 transition might not be thermal it has the same field dependence as in an optical experiments.

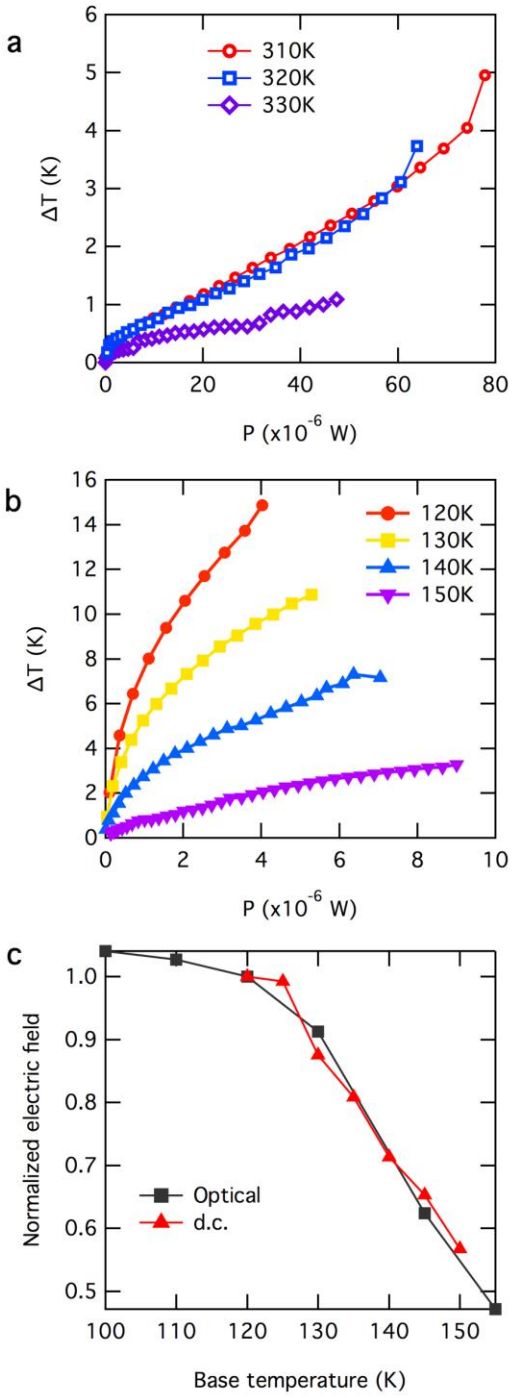

Figure 3.2: Using the RT curve (Fig. 3.1) as a thermometer we can assign a change in temperature in the device as a function of applied power (IV product). Results for V_2O_3 are in (a) and for VO_2 in (b). (c) Comparison of the normalized breakdown electric field vs base temperature for V_2O_3

To explain the nonlinear P-T characteristic, we calculated a steady state thermoelectric finite element method model in COMSOL Multiphysics. The model includes electric field and Joule heating effects and uses experimental data for resistivity as well as literature values for other material parameters[23,24]. For V_2O_3 we use an effective temperature model $T_{eff} = T_{loc} + \alpha E_{loc}$, where T_{loc} is the computed local temperature, E_{loc} is the computed electric field, and α is a fitted constant. This is inspired by the linear relationship between base temperature and threshold electric field in Fig 3.2c. Calculations were made for base temperatures of 310 K, 325 K, and 330 K for VO_2 devices and 120 K, 135K, and 150 K for V_2O_3 devices.

Temperature and current density profiles for the VO_2 device simulation with a base temperature of 310 K are presented on Fig. 3.3. Fig 3.3a shows the simulated IV characteristic with dashed lines indicating the current values at which the current density and temperature slices are plotted in Fig. 3.3(b-i). It can be seen that the current distribution is relatively homogenous throughout the bridge before the filament formation. However, once a critical current is reached, a filament spontaneously forms. This causes a drastic drop in the current density outside the filament and increase of three orders of magnitude in the current density inside the filament. The filament is largely confined to the surface (Fig 3.3h,i), penetrating less than 10 nm deep (with a similar width). Similar simulation results have been found for other base temperatures in VO_2 and V_2O_3.

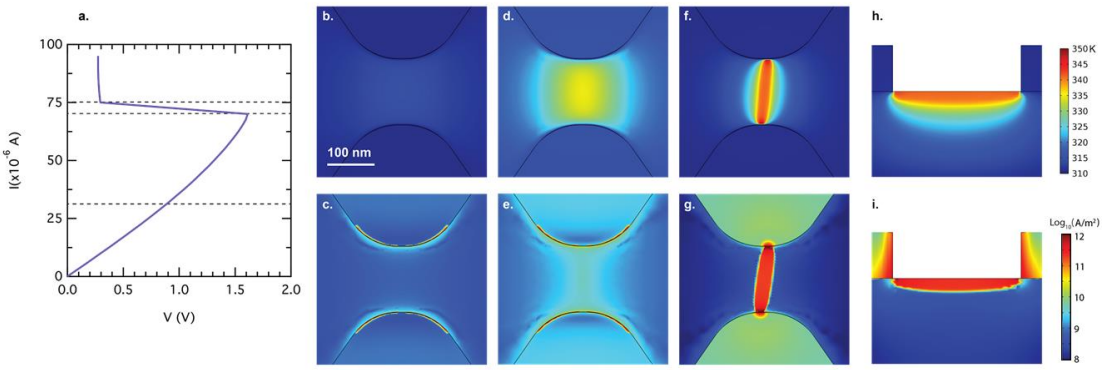

Figure 3.3: Steady state simulation of a VO_2 device with 310 K starting temperature at three different currents as indicated by the horizontal dash lines in the simulated IV curve in (a). Top (Bottom) panel corresponds to temperature (current density) maps for (b,c) 30, (d,e) 70 and (f,g) 75 uA. Top down view of the surface (h) current density and (i) temperature distribution as a function of applied current. The filament is not perfectly straight due to small symmetry breaking in the mesh.

Using the simulation results, we compute the PT and the IV characteristics similar to those shown for experimental results in Fig. 3.2. Fig. 3.4a, b show the simulated IV and PT characteristics of a VO_2 device that can be directly compared to experimental results in Fig 1d, Fig. 3.2a. The results are in qualitative agreement. In both Fig. 3.2a and Fig. 3.4b, the temperature-power characteristic is linear until 60 μW and then becomes superlinear. The main disagreement comes for the 330 K curve, which experimentally does not fall on top the 320 K and 310 K curves. This could be due to the presence of defects, which our simulation does not address. Fig. 3.4c shows qualitative agreements in the breakdown power as a function of base temperature between the simulation and the experiment. This suggests that the VO_2 current-induced transition can be explained by a Joule heating model.

Fig 3.4d, e show the simulated IV and PT characteristics of a V_2O_3 device. While a purely thermal model cannot reproduce our V_2O_3 results, by introducing an effective

temperature that is electric field dependent, we were able to reproduce the experimental results. From Fig 3.4f it can be see that the breakdown power in the simulation, just like in the experiment, increases as a function of increasing base temperature, something that could not occur in a simple Joule heating process.

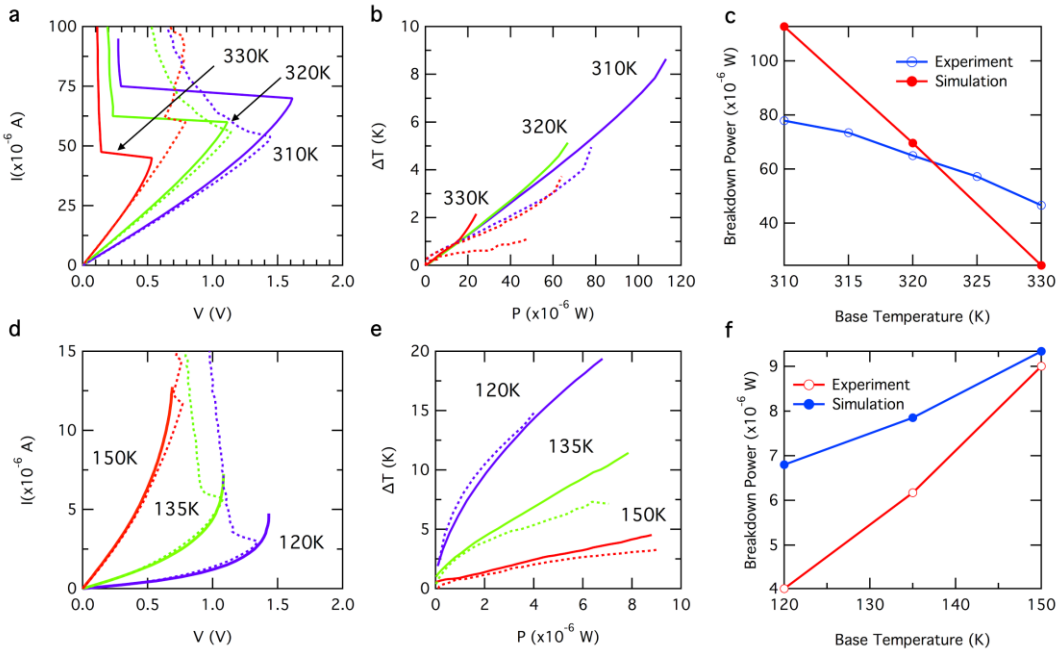

Figure 3.4: Observables obtained from the COMSOL simulation of VO_2 and V_2O_3 devices as a function of base temperature. Simulated VO_2 (a) I-V characteristic and (b) temperature -power characteristic. (c) Comparison of the simulation and experimental results for the MIT onset power. Simulated V_2O_3 (d) I-V characteristic and (e) temperature -power characteristic. (f) Comparison of the simulation and experimental results for the MIT onset power, note that there is strong disagreement both in the absolute value (experimental data multiplied by a factor of 10) and trend line. Dash lines in (a), (b), (d), and (e) correspond to the experimental data.

The difference between the VO_2 and V_2O_3 devices is likely due to a competition between electric field induced and Joule heating induced switching. Because dissipation scales with the square of device size, while heat production scales with the cube of device size, we believe that for smaller device sizes Joule heating transition will play an

increasingly smaller role. Furthermore, because V_2O_3 has an order magnitude larger base resistance, Joule heating is a factor of 9 less than in VO_2 for a given electric field. This is why in previous V_2O_3 device experiments[6,25], the transition appeared to be thermal while in our smaller devices the electronic transition occurs before the Joule heating transition.

The large thermal gradients (Fig. 3.3b, d) in the filaments cause large thermopower electric fields. Fig. 5 shows the generated electric field as a function of current for a VO_2 device. The temperature distribution is relatively even before the filament is established; however, once the filament is formed, the vanadium oxide outside the filament is cooled while the filament itself is strongly heated (Fig. 3.3). In the out-of-plane direction, assuming Seebeck coefficient for bulk VO_2 is ~150 μV/K [26], the thermopower electric field reaches 1.8 KeV/cm. Comparing to the applied field of 90 KeV/cm, the thermopower-induced electric field is about 2% of the driving field. This magnitude of induced field is not typical for nanodevices, with only comparable systems being non-local spin valves and carbon nanotubes[26–28]. Future experiments need to be design to experimentally verify the predicted large Seebeck fields.

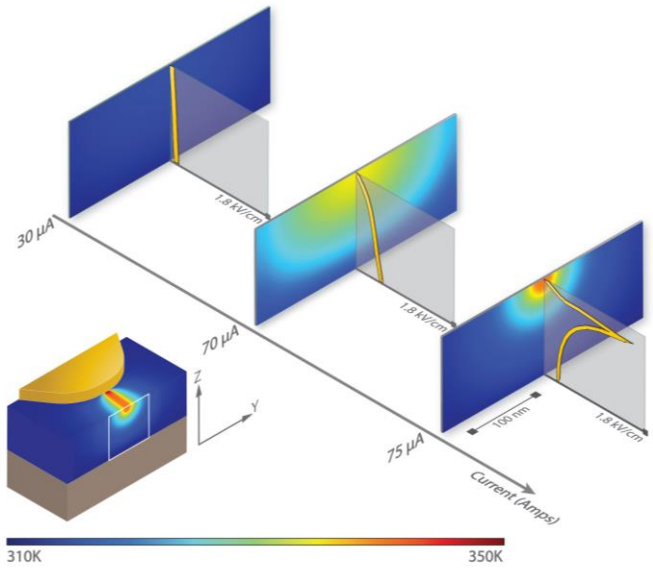

Figure 3.5. Seebeck electric field as a function of position in the filament at three applied currents (30 μA, 70 μA, and 75 μA). Inset shows the slice of the filament for which the fields were calculated.

We compared current induced MIT in VO_2 and V_2O_3 nanodevices at temperatures down to 30 K below MIT. We found that in VO_2 can be explained using a non-homogenous Joule heating finite element model. The conducting filament is mostly confined to the surface and has a very large temperature gradient (Fig 3.5) which is interesting for thermopower applications (induced electric field of about 10^3 V/cm). In V_2O_3, the transition has an electric field driven component that competes with the thermally driven transition. Because relative dissipation is larger for smaller device, as the device dimensions shrink the electric field transition mechanism starts to dominate. Our finding of an electric field driven transition in V_2O_3 can be leveraged for design of novel electronic and spintronic devices. It also opens a new avenue for searching for electric field driven MIT in VO_2 by further shrinking device size.

Acknowledgements

This chapter was prepared based on a paper that is to be submitted with the following author list: Ilya Valmianski, Siming Wang, Paul Wang, Juan Gabriel Ramirez, Stefan Guenon, Ivan K. Schuller. S.W, S.G., J.G.B. and I.K.S conceived of the idea. S.W, S.G., and I.V. prepared the samples and performed resistance measurements. I.V. and P.W. analyzed the data and proposed the theoretical model. All authors discussed the interpretation of the data. I.V., J.G.R., and P.W wrote the paper with input from all authors. The dissertation/thesis author was the primary investigator and author of this paper.

References

1. Zimmers, A., Aigouy, L., Mortier, M., Sharoni, A., Wang, S., West, K. G., Ramirez, J. G. & Schuller, I. K. Role of thermal heating on the voltage induced insulator-metal transition in VO_2. *Phys. Rev. Lett.* **110,** 56601 (2013).

2. Radu, I. P., Govoreanu, B., Mertens, S., Shi, X., Cantoro, M., Schaekers, M., Jurczak, M., De Gendt, S., Stesmans, a, Kittl, J. a, Heyns, M. & Martens, K. Switching mechanism in two-terminal vanadium dioxide devices. *Nanotechnology* **26,** 165202 (2015).

3. Markov, P., Marvel, R. E., Conley, H. J., Miller, K. J., Haglund, R. F. & Weiss, S. M. Optically Monitored Electrical Switching in VO_2. *ACS Photonics* **2,** 150805090843002 (2015).

4. Kruger, B. A., Joushaghani, A. & Poon, J. K. S. Design of electrically driven hybrid vanadium dioxide (VO_2) plasmonic switches. *Opt. Express* **20,** 23598–23609 (2012).

5. Guénon, S., Scharinger, S., Wang, S., Ramírez, J. G., Koelle, D., Kleiner, R. & Schuller, I. K. Electrical breakdown in a V_2O_3 device at the insulator-to-metal transition. *EPL (Europhysics Lett.* **101,** 57003 (2013).

6. Brockman, J. S., Gao, L., Hughes, B., Rettner, C. T., Samant, M. G., Roche, K. P. & ParkinStuart, S. P. Subnanosecond incubation times for electric-field-induced metallization of a correlated electron oxide. *Nat. Nanotechnol.* **9,** 453–458 (2014).

7. Qazilbash, M. M., Schafgans, A. A., Burch, K. S., Yun, S. J., Chae, B. G., Kim, B. J., Kim, H. T. & Basov, D. N. Electrodynamics of the vanadium oxidesVO2 and V_2O_3. *Phys. Rev. B* **77,** 115121 (2008).

8. Misochko, O. V., Tani, M., Sakai, K., Kisoda, K., Nakashima, S., Andreev, V. N. & Chudnovsky, F. A. Optical study of the Mott transition in V_2O_3. *Phys. Rev. B* **58,** 12789–12794 (1998).

9. Béteille, F. & Livage, J. Optical Switching in VO_2 Thin Films. *J. Sol-Gel Sci. Technol.* **921,** 915–921 (1998).

10. de la Venta, J., Wang, S., Ramirez, J. G. & Schuller, I. K. Control of magnetism across metal to insulator transitions. *Appl. Phys. Lett.* **102,** 122404 (2013).

11. De La Venta, J., Wang, S., Saerbeck, T., Ramírez, J. G., Valmianski, I. & Schuller, I. K. Coercivity enhancement in V_2O_3/Ni bilayers driven by nanoscale phase coexistence. *Appl. Phys. Lett.* **104,** (2014).

12. Saerbeck, T., de la Venta, J., Wang, S., Ramírez, J. G., Erekhinsky, M., Valmianski, I. & Schuller, I. K. Coupling of magnetism and structural phase transitions by interfacial strain. *J. Mater. Res.* **29,** 2353–2365 (2014).

13. Erekhinsky, M., De La Venta, J. & Schuller, I. K. Spin valve effect across the metal-insulator transition in V_2O_3. *J. Appl. Phys.* **114,** (2013).

14. Zhang, R., Wang, Z. S. Z. Z. L., Zhang, Z. D. Z. M., Dai, Z. G., Wang, L. L. L. L., Li, H. H.-J., Zhou, L., Shang, Y. X., He, J., Fu, D. J., Liu, J. J. J. R. J., Liu, H. W. H. H.-K. H. H. H., Wong, L. M., Wang, S. S. J., Tang, S. H., Zhang, X. X. X. X. H. X. X., Heckman, E. M., Gonzalez, L. P., Guha, S., A microscopic view on the Mott transition in chromium-doped V_2O_3. *Appl. Phys. Lett.* **14,** 1–5 (2014).

15. Hansmann, P., Toschi, A., Sangiovanni, G., Saha-Dasgupta, T., Lupi, S., Marsi, M. & Held, K. Mott-Hubbard transition in V_2O_3 revisited. *Phys. status solidi* **250,** 1251–1264 (2013).

16. Imada, M., Fujimori, A. & Tokura, Y. Metal-insulator transitions. *Rev. Mod. Phys.* **70,** 1039–1263 (1998).

17. Tanaka, A. Electronic Structure and Phase Transition in V_2O_3: Importance of 3d Spin-Orbit Interaction and Lattice Distortion. *J. Phys. Soc. Japan* **71,** 1091–1107 (2002).

18. Biermann, S., Poteryaev, A., Lichtenstein, A. I. & Georges, A. Dynamical singlets and correlation-assisted peierls transition in vo 2. *Phys. Rev. Lett.* **94,** (2005).

19. Sharoni, A., Ram'\irez, J. G. & Schuller, I. K. Multiple Avalanches across the Metal-Insulator Transition of Vanadium Oxide Nanoscaled Junctions. *Phys. Rev.*

Lett. **101,** 26404 (2008).

20. Wang, S., Ramírez, J. G. & Schuller, I. K. Avalanches in vanadium sesquioxide nanodevices. *Phys. Rev. B,* **92,** 85150 (2015).

21. McWhan, D. B., Menth, A., Remeika, J. P., Brinkman, W. F. & Rice, T. M. Metal-insulator transitions in pure and doped V_2O_3. *Phys. Rev. B* **7,** 1920–1931 (1973).

22. Abreu, E., Wang, S., Ramírez, J. G., Liu, M., Zhang, J., Geng, K., Schuller, I. K. & Averitt, R. D. Dynamic conductivity scaling in photoexcited V_2O_3 thin films. *Phys. Rev. B* **92,** 85130 (2015).

23. Kizuka, H., Yagi, T., Jia, J., Yamashita, Y., Nakamura, S., Taketoshi, N. & Shigesato, Y. Temperature dependence of thermal conductivity of VO_2 thin films across metal-insulator transition. *Jpn. J. Appl. Phys.* **54,** (2015).

24. Andreev, V. N., Chudnovskii, F. A., Petrov, A. V & Terukov, E. I. Thermal conductivity of VO_2, V_3O_5, and V_2O_3. *Phys. status solidi* **48,** K153–K156 (1978).

25. Guénon, S., Scharinger, S., Wang, S., Ramírez, J. G., Koelle, D., Kleiner, R. & Schuller, I. K. Electrical breakdown in a V_2O_3 device at the insulator-to-metal transition. *Europhys. Lett.* **101,** 57003 (2013).

26. Cao, J., Fan, W., Zheng, H. & Wu, J. Thermoelectric effect across the metal-insulator domain walls in VO_2 microbeams. *Nano Lett.* **9,** 4001–4006 (2009).

27. Bauer, G. E. W., Saitoh, E. & van Wees, B. J. Spin caloritronics. *Nat Mater* **11,** 391–399 (2012).

28. Maniwa, D. H. and T. U. and Y. N. and H. K. and Y. M. and T. Y. and T. S. and K. H. and Y. Thermoelectric properties of single-wall carbon nanotube films: Effects of diameter and wet environment. *Appl. Phys. Express* **9,** 25102 (2016).

Chapter 4 - Deviation from bulk in the pressure-temperature phase diagram of V_2O_3 thin films

We found atypical pressure dependence in the transport measurements of the metal to insulator transition (MIT) in epitaxial thin films of vanadium sesquioxide (V_2O_3). Three different crystallographic orientations and four thicknesses, ranging from 40 nm to 500 nm, were examined under hydrostatic pressures (P_h) of up to 1.5 GPa. All of the films at transition exhibited a four order of magnitude resistance change with transition temperatures ranging from 140 K to 165 K depending on the orientation. This allowed us to build pressure-temperature phase diagrams several orientations and film thicknesses. Interestingly, for pressures below 500 MPa, all samples deviate from bulk behavior and show a weak transition temperature (T_c) pressure dependence (dT_c/dP_h = $1.2x10^{-2}\pm0.3x10^{-2}$ K/MPa), which recovers to bulk-like behavior ($3.9x10^{-2}\pm0.3x10^{-2}$ K/MPa) at higher pressures. Furthermore, we found that pressurization leads to morphological but not structural changes in the films. This indicates that the difference in the thin film and bulk pressure-temperature phase diagrams is most probably due to pressure-induced grain boundary relaxation as well as both plastic and elastic deformations in film microstructure. These results highlight the difference between bulk and thin films behaviors.

The metal to insulator transition (MIT) in vanadium sesquioxide has been a topic of intense study. V_2O_3 has an unusual MIT because it coincides with a structural phase transition (SPT) and a magnetic phase transition (MPT) [1,2]. The co-occurrence of multiple phase transitions raises not only interesting questions about the underlying driving mechanisms, but also presents new opportunities for device applications such as infrared

imaging, spintronic devices, resistive switching devices, field-effect transistors, and magnetoelastically coupled recording media [3–8].

The MIT in V_2O_3 has been studied in vacuum as a function of temperature and applied voltage both in bulk and in thin films [2,9–12]. Furthermore , the pressure dependence of MIT has been studied in bulk in the $(V_{1-x}\ Cr_x)_2O_3$ system [13–15]. In this system, the MIT can be induced by decreasing the temperature (at sufficient small Cr concentration), by decreasing x or by increasing the pressure P. Studies have suggested that doping with Cr is equivalent to an applied pressure (x=0.01 corresponds to 4 kbar). The occurrence of the MIT and the SPT with a complex phase diagram suggests a coupling between electronic and lattice degrees of freedom. The question whether this coupling remains when the material is clamped to a substrate is of fundamental importance. For instance, in some materials, the pressure dependence deviates from its bulk behavior. This is mainly due to i) geometric anisotropy that arises when grain size is commensurate with the film thickness making the film quasi two-dimensional, ii) substrate clamping, that affects thin films under pressure by fixing their in-plane elastic response [16] or iii) complex thin film microstructure that can affect many properties by changing local strain [17–19]. All the above properties can be distinguished by studying the film response with pressure, varying either the film thickness or the film orientation. A detailed analysis of the pressure dependence of the MIT in V_2O_3 thin films was lacking in the literature, before the present studies.

In this paper, we present temperature-dependent transport measurements of V_2O_3 thin films under pressure as a function of both film thickness and crystallographic orientation in the low positive pressure regime (vacuum to 1.5 GPa), and compare them

to bulk measurements. We examine three different crystallographic orientations to investigate substrate clamping effects, and four different thicknesses to research geometric anisotropy and out of plane relaxation. Structural and morphological measurements before and after pressurization provide information on the microstructural changes due to pressurization.

V_2O_3 thin films were prepared in a high-vacuum sputter deposition system with base pressure of $1x10^{-7}$ Torr. All samples were grown on Al_2O_3 substrates. Four different film thicknesses: 40 nm, 60 nm, 100 nm, and 500 nm were prepared on (0 1 2) r-plane orientation of Al_2O_3. Furthermore, 100 nm V_2O_3 films were also grown on (1 0 0) m-plane and (1 1 0) a-plane Al_2O_3 orientations. All growth was performed at 750 ^oC in 4 mTorr of ultra-high purity (UHP) Ar by RF magnetron sputtering at 100 W of a V_2O_3 target. X-ray characterization including X-ray reflectivity (XRR) for thickness measurements as well as X-ray diffraction (XRD) and reciprocal space mapping (RSM) for structural measurements was carried out using a Rigaku Smartlab X-ray diffractometer. Fittings to the XRR data was done using MotoFit complex SLD fitting functionality[20] . The morphology of the thin films at room temperature was investigated with Veeco Scanning Probe Microscope operating in a tapping mode as an atomic force microscope (AFM).

Pressurization was performed at room temperature from atmospheric pressure to 1.5 GPa in a hydrostatic pressure cell Pcell 3000 from Almax EasyLab using a 5 ton press. Pentane was used as the pressure medium, which does not chemically interact with V_2O_3. Pressure was calculated using the resistance of a manganese manometer placed inside the cell, before and after the temperature scan. Resistance of the V_2O_3 film was

concurrently measured during pressurization. Both resistance measurements were performed in a pseudo-four probe configuration with a Keithley 6221A current source and Keithely 2181A nanovoltmeter. The applied pressure as measured by the press manometer was also recorded. This showed the expected linear relationship with the pressure as measured by the manganese manometer inside the cell.

The MIT measurements were performed by placing the pressurized Pcell 3000 into a Quantum Design PPMS-DynaCool with electrical contacts connected to an external Keithley 6221A current source and Keithely 2181A nanovoltmeter similar to the ones used during pressurization. A 100 nA constant current was applied and the voltage drop was measured. The low current was needed to accommodate the very large resistance change in the sample. The electrical transport measurement setup and the cryostat were controlled using a custom routine in National Instruments LabView software. The pressure cell was initially cooled at 10 K/min to a starting temperature well above the transition and then allowed to stabilize for an hour. To measure the cooling branch of the MIT, the temperature was decreased at a rate of 0.1 K/min to a final temperature below the MIT. Finally, the temperature was raised at 0.1 K/min to the starting temperature to measure the heating branch of the MIT. A slow temperature scan rate was used to minimize the internal thermal lag inside the pressure cell while measuring both decreasing and increasing temperature branches of the MIT. Once the full MIT hysteresis was measured, the pressure cell was heated to 300 K and left for an hour to stabilize. It was then removed from the cryostat and further pressurized to the next pressure value after which the resistance measurement process was repeated. Because of

possible pressure media leaks, the pressure cell cannot be depressurized to a controlled pressure (above atmosphere).

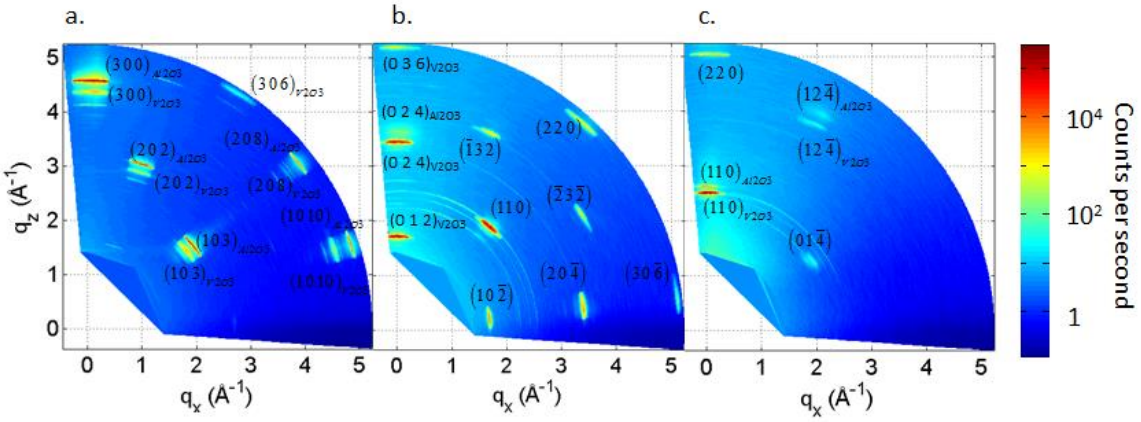

Figure 4.1: Reciprocal space maps for V_2O_3 100 nm films grown on different orientations of Al_2O_3. The data at $q_x = 0$ represents to the typical out-of-plane measurement. RSM for film grown on (a) a-plane (1 0 0) out-of-plane orientation. Both V_2O_3 and Al_2O_3 peaks are visible. Both in-plane and out-of-plane crystallographic orientations in V_2O_3 follow the Al_2O_3 orientations. Films grown on (b) r-plane (0 1 2) (sapphire peaks are not visible due to a slight miscut in the substrate) (c) m-plane (1 1 0). For the (2 2 0) plane only the V_2O_3 peak is visible because the Al_2O_3 peak is outside the scan range. In (b) and (c) faint polycrystalline rings (2-3 orders of magnitude more faint than the associated peaks) are visible suggesting that a small portion of the film is polycrystalline. The measurements were done without a monochromator to increase the overall diffraction intensity, which resulted in the presence of several contamination lines. The primary X-ray wavelength is 1.5406 Å associated with Cu Ka1, however significant contributions to the detected signal come from Cu Ka2 (λ = 1.5444 Å) and W L1 (λ = 1.0248 Å). For example, in Fig 3a, the (300) peak has another peak below the $(300)_{V2O3}$ associated with the W L1 of $(300)_{Al2O3}$, and an even more faint fourth peak from W L1 of $(300)_{V2O3}$.

Results of X-ray reciprocal space maps (RSM) of 100 nm V_2O_3 films grown on r-plane (0 1 2), m-plane (1 0 0) and a-plane (1 1 0) orientations of Al_2O_3 are shown in Fig. 4.1. All of the films follow the in-plane and out-of-plane crystallographic directions of the substrate and are thus epitaxial. This means that we can control which crystallographic orientation of V_2O_3 is unclamped when pressurized. The V_2O_3 lattice constants are identical to bulk values, within the resolution of the measurement system.

This is surprising since there is a lattice mismatch (a_{Al2O3} = 4.785 Å, a_{V2O3}= 4.9492 Å, c_{Al2O3} = 12.991 Å, c_{v2O3} = 13.9980 Å). A possible explanation is presence of an intermediate interfacial layer, as previously reported for VO_2 and other oxide heterostructures[21] or a weak overlayer-substrate interaction as present in many lattice mismatched epitaxial systems[22]. It is important to note that the elastic moduli for bulk V_2O_3 and Al_2O_3 are 400 GPa and 450 GPa respectively, with weak directional dependence. Furthermore, thin films tend to have larger elastic moduli than bulk, which means the V_2O_3 can be even harder.

The pressure and temperature dependences of the resistance of the thin films grown on the three different orientations are shown in Fig. 4.2. All of the films present a MIT with roughly four orders of magnitude resistance change and display a thermal hysteresis between the cooling and warming branches of about 10 K. The transition temperature of the MIT is defined as the inflection point in the logarithm of the resistance of the cooling branch. We chose the cooling branch to avoid a possibility of minor loops in the hysteresis. All of the measurements start with the sample at room temperature (at which pressurization occurs) where the material is in the metallic state. Then, the film is monotonically cooled into the insulating state, and, after reaching the minimum temperature, it is warmed back to room temperature. Once at room temperature the pressure in the pressure cell is increased, and the temperature scan is repeated.

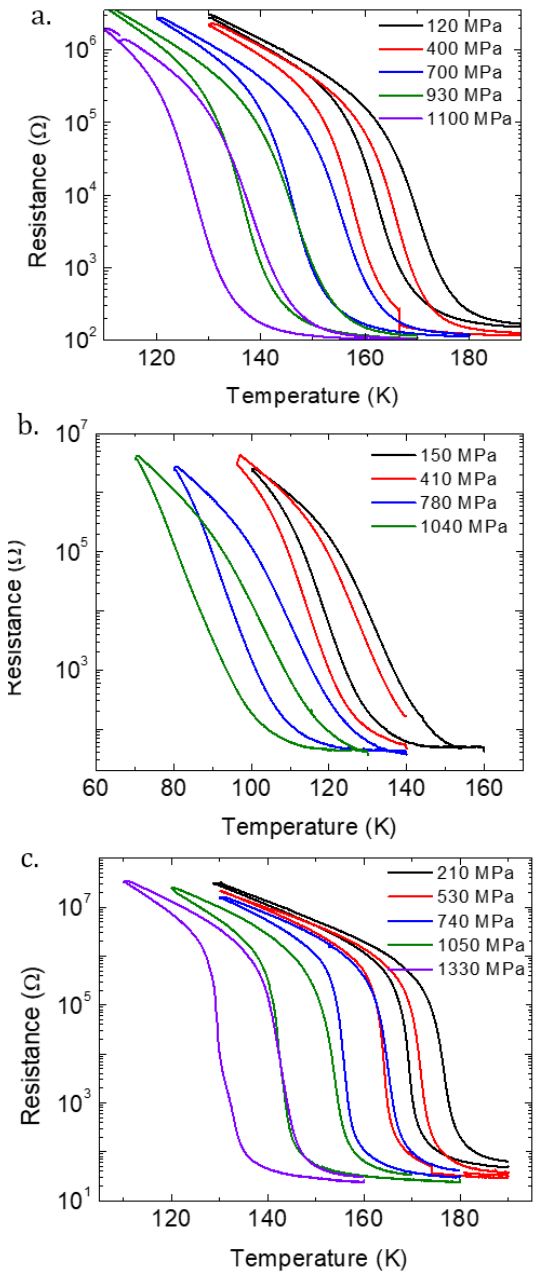

Figure 4.2: Resistance vs. temperature dependence at different pressures for (a) r-plane (b) a-plane, and (c) m-plane. The transition temperature decreases monotonically with increased pressure. Only absolute resistance measurements are reported because the samples were small (<1 mm^2) and the variation in the geometry of the indium contact point made accurate evaluation of resistivity across sample difficult. However, the magnitude and shape of transition is comparable or better to those previously reported in literature (larger change, sharper transition) [18,23]. The difference in shape of the curves can be attributed to interfacial microstructure[18,24].

The cooling and heating branches do not close at low temperature because of the persistence of micro-inclusions of metallic domains in the insulating phase even after most of the transition has occurred. This has been previously observed using FORC measurements in VO_2[25]. The substrate dependence of the transition temperature and hysteresis loop shape has also been observed under vacuum measurements and was attributed to two factors[18,23]. First, different Al_2O_3 substrate orientations substrates have different surface terracing. The resulting morphology generates strain in the V_2O_3 grains, which can be modified by annealing the substrate before growth. Second, different substrate orientations have different lattice mismatches. These two factors are also the reason why it is very difficult to grow V_2O_3 with several orders of magnitude MIT on c-cut (1 0 0) Al_2O_3 [18].

XRD patterns and AFM images before and after the pressurization are shown in Fig. 4.3. Fig. 4.3a shows the (0 1 2) Bragg peak of a 100 nm V_2O_3 grown on r-plane Al_2O_3, before and after pressurization. There is no change in the peak position, which suggests that there are no structural changes. Fig. 4.3b shows an AFM image of the same film. Analysis of the latter for pressure effects on the microstructure reveals changes in roughness. For example, for this particular sample, 3 areas several millimeters apart, were measured before and after pressurization.

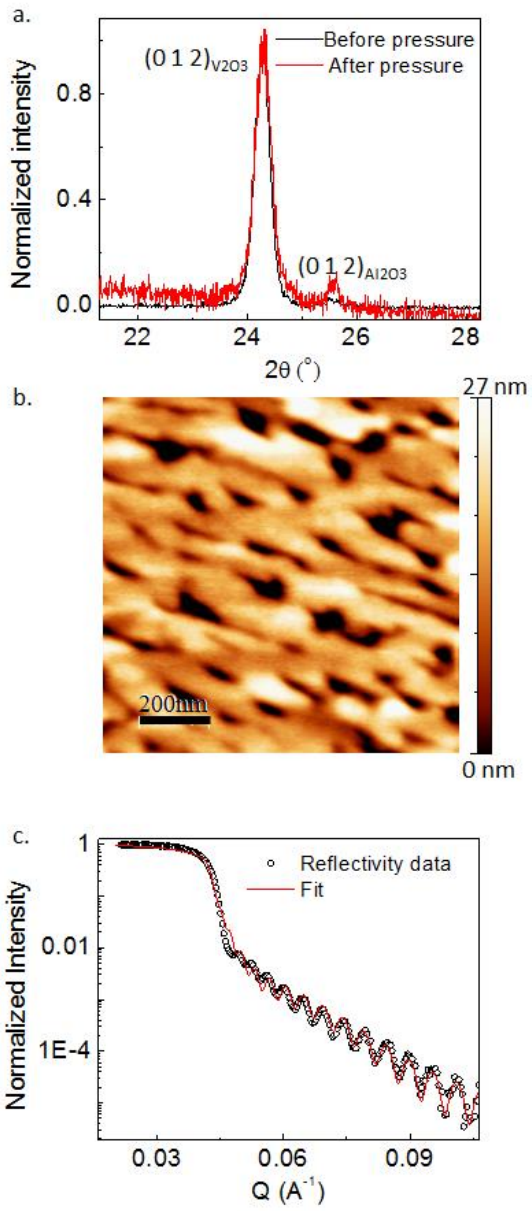

Figure 4.3: Structural and microstructural characterization of a 100 nm V_2O_3 thin film grown on r-plane Al_2O_3: (a) XRD of the (0 1 2) out of plane peak before and after pressurization. Since the pressure cell accepts only very small sample sizes (less than 1x1 mm^2), the pattern after pressurization is noisier (b) AFM image after pressurization (c) XRR data, and fit of data, before pressurization ($\chi^2 = 0.0198$). Reflectivity data after pressurization not shown since is very noisy.

The root-mean-square roughness changes from 7.5 nm before to 6.1 nm after pressurization ($p<0.001$). This suggests that while pressurization does not induce atomic scale structural changes, it does cause microstructural changes. Furthermore, the numerous morphological indentations seen in the AFM image can yield additional mechanisms for strain relaxation. Fig. 4.3c shows XRR with a fit for nominally 100 nm thick V_2O_3 film grown on r-plane Al_2O_3. The fit is performed by using a two-layer model with a 100 nm bottom layer (1 nm roughness) and an 8 nm top layer (3.3 nm roughness) with lower density on top of a 1.2 nm rough substrate. The top layer is likely oxygen oversaturated due to exposure to air. The differences between the fit and the data in the low-Q range are probably due to the top layer having a non-uniform electron scattering length density (eSLD). The real part of the eSLD is linearly proportional to the material density. The fitted real part of the eSLD of the bottom layer of the 100 nm film is $(36.2 \pm 0.2)\cdot 10^{-6}/Å^2$, as compared to the nominal value of $38.8\times 10^{-6}/Å^2$ for the bulk counterpart. Literature values of the imaginary component of the eSLD were used[26]. This strongly implies that the V_2O_3 thin film has a density 6.6% lower than the bulk material.

The pressure-temperature phase diagrams extracted from the transport measurements in Fig. 4.3 are displayed in Fig. 4.4. Fig. 4.4a shows that different crystal orientations have different transition temperatures. M-plane and r-plane oriented films have transition temperatures consistently above that of the bulk material, while the a-plane oriented film has a transition temperature below the bulk material. Fig. 4.4b shows the phase diagram for different thicknesses: 40 nm, 60 nm, 100 nm, and 500 nm thick films grown on r-plane sapphire. The 40 nm film shows a transition temperature shifted to lower temperatures. This is because the film thickness is lower than the lateral grain

size, which possibly affects the long-range order responsible for the MIT. Furthermore, at lower thicknesses interfacial effects become more predominant. The 100 nm and 500 nm thick films show nearly identical behavior since their thickness is larger than the lateral grain size. At room temperature, the boundaries expected are only low-angle grain boundaries[27]. At low temperature, below the MIT, additional boundaries appear due to crystal twining.

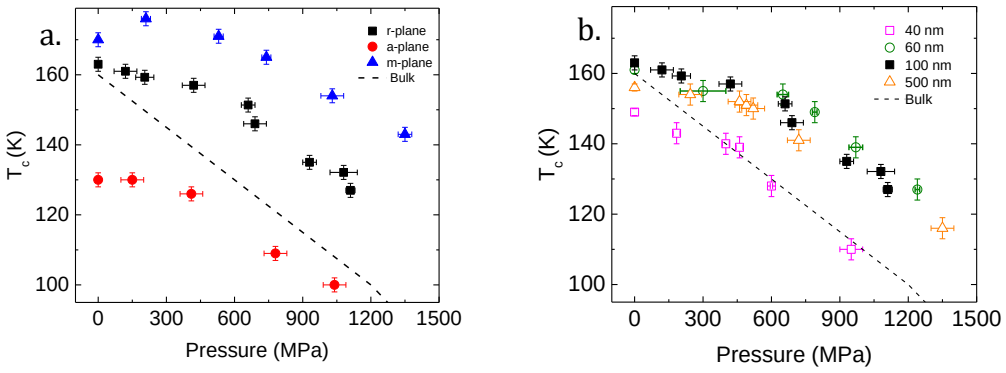

Figure 4.4: Transition temperature as a function of pressure. In both panels, the dashed line represents the experimental single crystal bulk behavior[28]. (a) Phase diagrams plotted as a function of crystallographic orientation for 100 nm thin films. (b) Phase diagrams plotted as a function of film thickness for r-cut sapphire. The uncertainty in pressure was determined from a pressure measurement before and after the temperature sweep. The 3K uncertainty in transition temperature is a worst case uncertainty in the location of the inflection point in the curve.

The most striking result appears when a constant T-offset is subtracted from each of the curves in Fig. 4.4. The new pressure dependences are shown in Fig. 4.5: the pressure dependence of all samples grown on different orientation substrates and with different thicknesses collapse onto two single master lines that significantly deviate from the bulk behavior. Thin films present two pressure dependence regimes. Below 500 MPa, a weaker pressure dependence than in bulk is observed, with a critical temperature-

pressure slope of $1.2x10^{-2}$ K/MPa.

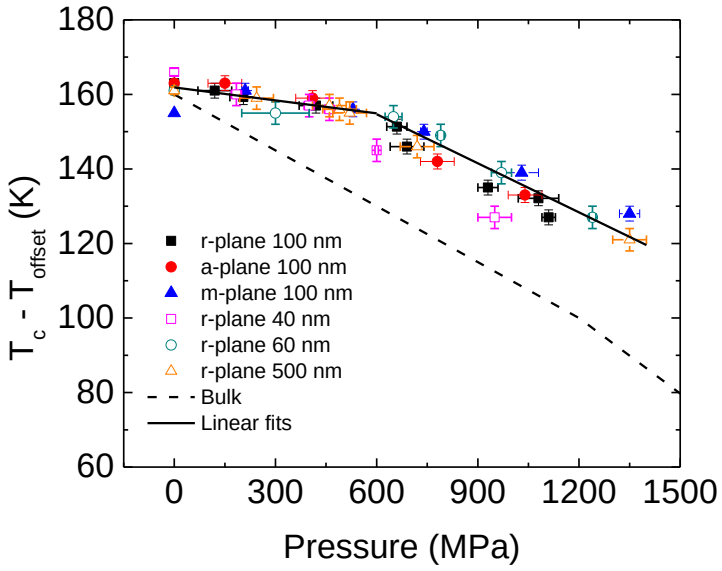

Figure 4.5: Transition temperature as a function of pressure, with a constant T-offset subtracted from each of the phase diagrams in Fig 4. All data collapse onto two master lines (below 600 MPa, slope -0.012±0.003 K/MPa, above 600 MPa -0.039±0.003 K/MPa); a *small slope region* and a *large slope region*. Dashed line represents the experimental single crystal bulk behavior with a slope of -0.05 K/MPa [28].

This region is referred to as the *small slope regime*. In contrast, above 500 MPa the pressure dependence is similar to the bulk behavior with a temperature-pressure slope of $3.9x10^{-2}$ K/MPa, which we refer to as the *large slope regime*. Moreover, the difference between large and small slope regimes is much more pronounced than the variation of the V_2O_3 thin film behavior with either crystallographic orientation or thickness, which suggest that they are physically relevant.

We propose that the two-slope regime is due to the effective porosity of the films. As observed in the AFM images (Fig. 4.3b) and XRR data (Fig. 4.3c), the films are not uniformly dense, which allows for reversible grain boundary relaxation when pressurized. As the films are epitaxial (Fig. 4.1), they are clamped to the substrate and relax back to

the porous state when the pressure is removed. The small morphological changes seen in the AFM images are due to small plastic deformations in the relaxation process.

This mechanism has been extensively studied for foam materials, which also exhibit a kink in their stress-strain dependence, showing a low stress dependence at low pressure and bulk-like behavior at high pressure[29–31]. In fact, qualitatively the change in slope in Fig. 5 is consistent with a simple model that assumes the pressure to be isotropic in the substrate and the film to be experiencing a reduced in plane pressure due strain relaxation within boundaries. Then, with increasing pressure, the relaxation mechanism become exhausted and the film behaves bulk-like[32].

Pressure-dependent measurements help understanding the nature of the MIT and the SPT in V_2O_3. The thin film dependence of V_2O_3 in the application-relevant low positive pressure regime between 0 and 1.5 GPa is reported. We have found that transition temperature of V_2O_3 thin films show two pressure dependencies; smaller than in bulk below 500 MPa, and similar to bulk, above 500 MPa. This feature is unique to all thin films measured in this work and has not been observed in the bulk counterpart. Furthermore, the effect is largely independent of film orientation or thickness. This is likely because the films are not fully compact (thin film density is 6.6% lower than bulk value) and undergo strain relaxation when pressurized. This strain relaxation occurs both in grain boundaries and in morphological defects in the film. When the stress relaxation mechanisms become exhausted, the behavior of the film becomes the same as in bulk. These findings are further supported by the fact that there are no structural changes in the films before and after pressurization, while there is a slight change in the film

microstructure. This is especially relevant for developing SPT-based heterostructure devices since they often operate through elastic coupling with the V_2O_3 layer.

Acknowledgements

This chapter reproduces in full the following paper: Ilya Valmianski, Juan Gabriel Ramirez, Christian Urban, Xavier Batlle, and Ivan K. Schuller "Deviation from bulk in the pressure-temperature phase diagram of V_2O_3 thin films" Phys. Rev. B 95, 155132 (2017). I.V, J.G.B, and C.B fabricated and measured all samples. I.V. performed the analysis of the data. I.V. and J.G.B. wrote the paper with input from all authors. The dissertation author was the primary investigator and author of this paper.

References

1. Imada, M., Fujimori, A. & Tokura, Y. Metal-insulator transitions. *Rev. Mod. Phys.* **70,** 1039–1263 (1998).

2. Sass, B., Tusche, C., Felsch, W., Quaas, N., Weismann, A. & Wenderoth, M. Structural and electronic properties of epitaxial V_2O_3 thin films. *J. Phys. Condens. Matter* **16,** 77 (2004).

3. Ruzmetov, D., Gopalakrishnan, G., Ko, C., Narayanamurti, V. & Ramanathan, S. Three-terminal field effect devices utilizing thin film vanadium oxide as the channel layer. *J. Appl. Phys.* **107,** 114516 (2010).

4. Yang, Z., Ko, C. & Ramanathan, S. Oxide electronics utilizing ultrafast Metal-Insulator transitions. *Annu. Rev. Mater. Res.* **41,** 337–367 (2011).

5. Sharoni, A., Ramirez, J. G. & Schuller, I. K. Multiple Avalanches across the Metal-Insulator transition of vanadium oxide nanoscaled junctions. *Phys. Rev. Lett.* **101,** 26404 (2008).

6. Sass, B., Tusche, C., Felsch, W., Bertran, F., Fortuna, F., Ohresser, P. & Krill, G. Magnetic and electronic interaction effects at the interfaces of Fe⁄V_2O_3 and Co⁄V_2O_3 bilayers. *Phys. Rev. B* **71,** 14415 (2005).

7. Lupi, S., Baldassarre, L., Mansart, B., Perucchi, A., Barinov, A., Dudin, P., Papalazarou, E., Rodolakis, F., Rueff, J.-P., Itié, J.-P., Ravy, S., Nicoletti, D., Postorino, P., Hansmann, P., Parragh, N., Toschi, A., Saha-Dasgupta, T., Andersen, O. K., Sangiovanni, G., A microscopic view on the Mott transition in

chromium-doped V_2O_3. *Nat. Commun.* **1,** 105 (2010).

8. Saerbeck, T., de la Venta, J., Wang, S., Ramírez, J. G., Erekhinsky, M., Valmianski, I. & Schuller, I. K. Coupling of magnetism and structural phase transitions by interfacial strain. *J. Mater. Res.* **29,** 2353–2365 (2014).

9. Zimmers, A., Aigouy, L., Mortier, M., Sharoni, A., Wang, S., West, K. G., Ramirez, J. G. & Schuller, I. K. Role of thermal heating on the voltage induced Insulator-Metal transition in VO_2. *Phys. Rev. Lett.* **110,** 56601 (2013).

10. Guénon, S., Scharinger, S., Wang, S., Ramírez, J. G., Koelle, D., Kleiner, R. & Schuller, I. K. Electrical breakdown in a V_2O_3 device at the insulator-to-metal transition. *EPL* **101,** 57003 (2013).

11. Brockman, J., Aetukuri, N. P., Topuria, T., Samant, M. G., Roche, K. P. & Parkin, S. S. P. Increased metal-insulator transition temperatures in epitaxial thin films of V_2O_3 prepared in reduced oxygen environments. *Appl. Phys. Lett.* **98,** 152105 (2011).

12. Jeong, J., Aetukuri, N., Graf, T., Schladt, T. D., Samant, M. G. & Parkin, S. S. P. Suppression of Metal-Insulator Transition in VO_2 by Electric Field Induced Oxygen Vacancy Formation. *Science (80).* **339,** 1402–1405 (2013).

13. McWhan, D. B., Remeika, J. P., Rice, T. M., Brinkman, W. F., Maita, J. P. & Menth, A. Electronic Specific Heat of Metallic Ti-Doped V_2O_3. *Phys. Rev. Lett.* **27,** 941–943 (1971).

14. Carter, S. A., Rosenbaum, T. F., Lu, M., Jaeger, H. M., Metcalf, P., Honig, J. M. & Spalek, J. Magnetic and transport studies of pure V_2O_3 under pressure. *Phys. Rev. B* **49,** 7898–7903 (1994).

15. Kuwamoto, H., Honig, J. M. & Appel, J. Electrical properties of the $(V_{1-x}Cr_x)_2O_3$ system. *Phys. Rev. B* **22,** 2626–2636 (1980).

16. Bud'ko, S. L., Guimpel, J., Nakamura, O., Maple, M. B. & Schuller, I. K. Uniaxial pressure dependence of the superconducting critical temperature in $Ba_2Cu_3O_{7-d}$ high-T_c oxides. *Phys. Rev. B* **46,** 1257–1260 (1992).

17. Jang, H. W., Kumar, A., Denev, S., Biegalski, M. D., Maksymovych, P., Bark, C. W., Nelson, C. T., Folkman, C. M., Baek, S. H., Balke, N., Brooks, C. M., Tenne, D. A., Schlom, D. G., Chen, L. Q., Pan, X. Q., Kalinin, S. V, Gopalan, V. & Eom, C. B. Ferroelectricity in strain-free $SrTiO_3$ thin films. *Phys. Rev. Lett.* **104,** 197601 (2010).

18. Brockman, J., Samant, M. G., Roche, K. P. & Parkin, S. S. P. Substrate-induced disorder in V_2O_3 thin films grown on annealed c-plane sapphire substrates. *Appl. Phys. Lett.* **101,** 51606 (2012).

19. Wong, A. T., Beekman, C., Guo, H., Siemons, W., Gai, Z., Arenholz, E., Takamura, Y. & Ward, T. Z. Strain driven anisotropic magnetoresistance in antiferromagnetic $La_{0.4}Sr_{0.6}MnO_3$. *Appl. Phys. Lett.* **105,** 52401 (2014).

20. Nelson, A. Co-refinement of multiple-contrast neutron/X-ray reflectivity data using MOTOFIT. *J. Appl. Crystallogr.* **39,** 273–276 (2006).

21. Pennycook, S. J., Zhou, H., Chisholm, M. F., Borisevich, A. Y., Varela, M., Gazquez, J., Pennycook, T. J. & Narayan, J. Misfit accommodation in oxide thin film heterostructures. *Acta Mater.* **61,** 2725–2733 (2013).

22. Dong, L., Schnitker, J., Smith, R. W. & Srolovitz, D. J. Stress relaxation and misfit dislocation nucleation in the growth of misfitting films: A molecular dynamics simulation study. *J. Appl. Phys.* **83,** 217 (1998).

23. Allimi, B. S., Alpay, S. P., Xie, C. K., Wells, B. O., Budnick, J. I. & Pease, D. M. Resistivity of V_2O_3 thin films deposited on a-plane (110) and c-plane (001) sapphire by pulsed laser deposition. *Appl. Phys. Lett.* **92,** 202105 (2008).

24. Schuler, H., Klimm, S., Weissmann, G., Renner, C. & Horn, S. Influence of strain on the electronic properties of epitaxial V_2O_3 thin films. *Thin Solid Films* **299,** 119–124 (1997).

25. Ramírez, J. G., Sharoni, A., Dubi, Y., Gómez, M. E. & Schuller, I. K. First-order reversal curve measurements of the metal-insulator transition in VO_2: Signatures of persistent metallic domains. *Phys. Rev. B - Condens. Matter Mater. Phys.* **79,** 235110 (2009).

26. Sears, V. F. Neutron scattering lengths and cross sections. *Neutron News* **3,** 26–37 (1992).

27. De La Venta, J., Wang, S., Saerbeck, T., Ramírez, J. G., Valmianski, I. & Schuller, I. K. Coercivity enhancement in V_2O_3/Ni bilayers driven by nanoscale phase coexistence. *Appl. Phys. Lett.* **104,** (2014).

28. Jayaraman, A., McWhan, D. B., Remeika, J. P. & Dernier, P. D. Critical Behavior of the Mott Transition in Cr-Doped V_2O_3. *Phys. Rev. B* **2,** 3751–3756 (1970).

29. Triawan, F., Kishimoto, K., Adachi, T., Inaba, K., Nakamura, T. & Hashimura, T. The elastic behavior of aluminum alloy foam under uniaxial loading and bending conditions. *Acta Mater.* **60,** 3084–3093 (2012).

30. Petel, O. E., Ouellet, S., Higgins, A. J. & Frost, D. L. The elastic-plastic behaviour of foam under shock loading. *Shock Waves* **23,** 55–67 (2013).

31. McCullough, K. Y. G., Fleck, N. A. & Ashby, M. F. Uniaxial stress–strain behaviour of aluminium alloy foams. *Acta Mater.* **47,** 2323–2330 (1999).

Chapter 5 – Conclusion and outlook

Vanadium oxides are an important family of highly correlated oxides with many interesting properties. The two oxides I have studied in particular, V_2O_3 and VO_2, undergo simultaneously both a structural phase transition and a metal to insulator transition. Canonically, in V_2O_3, the MIT is a Mott transition with a Slater-like antiferromagnetic ordering, while, in VO_2, there is dimerization due to a Peierls transition, with some on-site repulsion and no change in magnetism. Both materials have a highly inhomogeneous transition resulting in a large region of coexistence of both metallic and insulating domains. In my thesis, I have studied the transitions in vanadium oxides through three related modalities: ultra-fast time scales (Chapter 2), small length scales (Chapter 3), and under strain (Chapter 4). Each of these experimental modalities reveal something new about the nature of the transition and all of them point to the importance of length scale competitions and material inhomogeneity.

In Chapter 2, we studied the effect of photoexcitation on the structure of V_2O_3 at ultra-fast times using X-ray pump-probe experiment at SLAC Linear Coherent Light Source. We observed a metastable structural phase that forms during a photoexcited insulator to metal transition on a 2 ps timescale. The new phase is due to electron delocalization in a structurally inhomogeneous lattice. This allows some of the low temperature monoclinic cells to decrease their tilt returning to a rhombohedral symmetry, increasing the overall structural correlation length. They key finding is a length scale competition between monoclinic and rhombohedral domains which can be pushed toward rhombohedral symmetry using photoexcitation and may be related to the underlying electronic correlation lengths. Furthermore, our findings provide some evidence that this

symmetry change, without the lattice constant change, is actually a second order transition. This raises a question of whether equilibrium V_2O_3 structural phase transition also occurs in a two-step process, with a second order symmetry changed followed by a first order lattice constant change.

In Chapter 3, we studied the effect of device length scale on the current induced transition in VO_2 and V_2O_3. We found that the transition mechanism is different n VO_2 and V_2O_3 devices and developed an inhomogeneous thermoelectric model that explains the behavior of both materials. We found that the devices do not transition simply because of Joule heating induced rise in temperature or applied local electric field but as a combination of both effects. We defined an effective local temperature, which is a sum of true local temperature and the scaled magnitude of the local electric field. With this insight we were able to quantitatively explain the behavior of both VO_2 and V_2O_3 using a high spatial resolution finite element methods model. We found that the reason previous studies mostly sided with either Joule heating or electric field effects as being responsible for the current induced transition is because there is a competition of length scales. As device size shrinks relative dissipation increases and electric field effects become more pronounced. Another important prediction we made is the presence of high Seebeck fields in our devices. Because the transition is highly inhomogeneous and occurs through filament formation, Seebeck electric fields on the order of 1000 V/cm are generated.

In Chapter 4, we studied the effect of pressure and strain on the phase transition of V_2O_3. Electrical properties were measured as a function of film thickness (40-300 nm) and substrate orientation (r-, a-, and m- plane) at applied hydrostatic pressures of up to 1.5 GPa. We found that there is a deviation from bulk behavior due to morphological

inhomogeneity in the film. Small creases in the film grain boundaries act as effective relaxation points, dramatically decreasing strain under 500 MPa. However, above that threshold all of the pressure is transmitted through the film. Remarkably, this 500 MPa threshold is mostly independent of thin film thickness and orientation.

There are still many interesting topics to be studied in vanadium oxides. From our photo induced SPT studies, we have learned about ultrafast timescale symmetry changes in the out-of-plane geometry. However, it is important to invetigate the in-plane geometry. Another direction of research is to carefully analyze long time scale data. We have preliminarily researched up to 500 ps delays and found that the structural transition has a different functional time dependence from previous electronic measurements. This suggests that on those time scales there may be a decoupling of structural and electronic transition. This may be especially interesting because of our insight on the two-step nature of the transition. While the structural transition looks like it has both a second order phase transition step and a first order phase transition step, the Mott electronic transition should be purely first order.

From our electrical transport in nanodevices studies we have developed a robust electrothermal model to predict all kinds of VO_2 and V_2O_3 devices. An immediate further validation can be made by studying a set of varying length scale devices of up to 1 μm. Our model predicts a crossover from majority-electric to majority-Joule heating driven transition mechanism. Furthermore, additional work can be done by downscaling VO_2 devices to find if a purely electrically driven transition is possible.

Finally, from the pressure studies we found the importance of morphological defects in strain relaxation in V_2O_3. Preliminary studies by Dr. Christian Urban also

reveal that adding metallic layer on top of V_2O_3 can prevent these relaxation mechanisms. This is particularly interesting in that it opens up avenues for strain engineering in V_2O_3 and, thus, gives a new "knob" for control of the phase transitions. Potential interest lies in how this can be combined with heat-assisted magnetic recording (HAMR) as we have also previously shown large strain based coercivity enhancement in V_2O_3/Ferromagnet bilayers.

Looking at materials through the window of "small, fast, and strained" allows us an unprecedented view into material physics. For vanadium oxides we have observed many length scale and time scale competitions and the importance of inhomogeneity in almost all of the electronic and structural properties. Using inhomogeneity for novel device and material engineering is an important challenge for upcoming research and there are many promising avenues that my research has opened up -- from controlling strain though bilayer coupling, to length scale tuning of nanodevices and spatially inhomogeneous metastable transitions during photoexcitation.

Appendix A – Supplemental material for chapter 3

100 nm V_2O_3 and VO_2 thin films were grown using magnetron sputter deposition as described in Chapter 1. Film structure was verified with X-ray diffraction (Rigaku Smartlab Diffractometer), which showed that the films were highly textured in both out-of-plane and in-plane directions. The devices were fabricated on the films using a three-step lithographic process. First, 20 um x 50 um vanadium oxide islands were defined with negative-resist photolithography. Vanadium oxide outside of the islands was etched with reactive ion etching with Oxford Instruments P80 RIE system. The etching was performed for 2 minutes under 40 mTorr pressure with 50 sccm Cl_2 and 10 sccm Ar flow at 200 W. In the second lithographic step, triangular electrodes were defined using e-beam lithographic system Raith50 with 950PMMA C4 positive resist. Exposure doses ranged between 270 and 330 $\mu C/cm^2$ to adjust the gap size to the desired value of 140 x 200 nm. The electrodes were deposited by e-beam physical vapor deposition with a 20 nm of V adhesion layer followed by an 80 nm Au layer at a rate of 1 A/s. Finally, positive resist (S1818) photo-lithography was used to define larger electrodes and connection pads. The devices were inspected by scanning electron microscopy (SEM). An example of the device is presented in the inset of Fig. 1a.

Electrical measurements were performed in a two-probe configuration using Keithley 6221A current source and Keithley 2181A nanovoltmeter in a closed cycle cryostat. Two types of electrical measurements were performed. Resistance-temperature characteristic was measured with a fixed current of 100 nA, which is significantly below the threshold needed to induce a metal-insulator transition. Current-voltage characteristic was measured by slowly ramping up the current to 200 μA. Each measurement was

performed in a series of ten at a sampling rate of 5 Hz, to ensure reproducibility. R-T curves were taken at a temperature ramp rate of 1 K/min. Example R-T characteristic of a VO_2 and V_2O_3 device are presented in Fig 1.

We perform steady state finite element simulations using COMSOL Multiphysics. Our model incorporates the Joule heating module which couples electrodynamics and heat transfer physics. The dimensions of the simulated device reflect that of the fabricated device with material properties taken from literature. Conductivity of the metal-oxide was optimized to the R-T curve obtained experimentally from our devices.

Because the conductivity of vanadium oxides is temperature dependent, the partial differential equation becomes nonlinear. In addition, conductivity changes by several orders of magnitude within a few degrees kelvin resulting in bifurcations. This phenomenon is reflected experimentally by a spontaneous formation of a filament at critical power as current is slowly ramped.

To solve the coupled equations and address bifurcations of the system, we implement an iterative method in COMSOL where a constantly damped Newtonian step is taken each iteration. This method continues until the solution's relative error is less than 10^{-4} for all dependent variables, upon which we consider the solution sufficiently converged. In addition, multiple spatially independent solutions exist satisfying boundary conditions. For this paper, we include the solution where the filament nucleates near the middle of the channel.

Appendix B – Supplemental material for chapter 4

We propose a simple model to qualitatively explain the kink in the pressure dependence of the critical temperature in V_2O_3. In this model the V_2O_3 grains are represented as trapezoidal prisms packed in a square lattice (Fig B1).

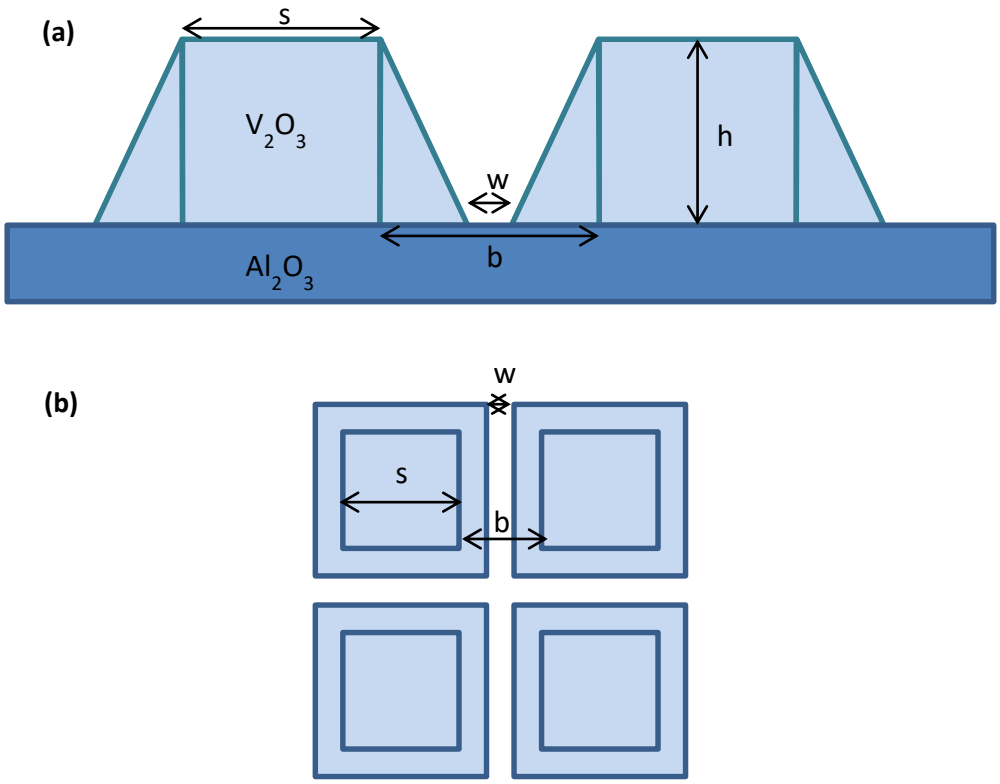

Figure B.1: (a) Side view (b) top view of the simplified V_2O_3 grain structure model. The grain length scale is then *s*, while the grain boundary thickness is *b*, while near the substrate there is an additional gap area (with length scale *w*).

While there is a thin strain relaxation layer in between the substrate and the film (on the order of interface roughness, ~1nm) that is clamped, the V_2O_3 grains on top of this layer can effectively shift laterally by expanding in the gaps between grains, without moving their center of mass. As the pressure is applied the effective in plane stress in the film is lower than the applied hydrostatic pressure, and the gaps between V_2O_3 grains

shrink. At 500 MPa, where a kink in the dT_c/dP occurs, the gaps between grains disappear and V_2O_3 starts to behave like a bulk material.

Apart from grain geometry we make the following additional assumptions:

- Al_2O_3 substrate is isotropic and is subject to hydrostatic pressure
- V_2O_3 film is isotropic, when there is still gaps between grains ($w>0$) there is a reduced in-plane pressure p_{red} and an out of plane pressure $p_o=p_{hydrostatic}$
- As the pressure is applied, V_2O_3 expands faster than Al_2O_3 substrate so the gaps between grains close. Once they close the in plane pressure becomes the same as the hydrostatic pressure (this is why at above the kink pressure (p_k = 500 MPa) V_2O_3 film behaves like bulk.
- The T_c is linearly proportional with the unit cell length scale (this is supported by the fact that dT_c/dP is linear) so we can estimate the ratio of $(dT_c/dP)_{\text{before kink}}/(dT_c/dP)_{\text{after kink}}$ as equal to $(dl/dP)_{\text{before kink}}/(dl/dP)_{\text{after kink}}$

We find that given our model:

- The reduced in-plane pressure in V_2O_3 at the location of the kink is 96 MPa
- The expected ratio of slopes is 2.19, which is somewhat smaller than the observed value of 3.25

B.1 Boundary relaxation length scale

The volume of a unit cell as shown on Fig 1 is

$$V_{film} = h\left(s^2 + s(b-w) + \frac{1}{4}(b-w)^2 \right) \tag{0.1}$$

Where *s* is the size of the V_2O_3 grain (as found from AFM, for example), *b* is the boundary between grains, *h* is the thickness of the film, and *w* is the distance on the substrate surface between grains. The volume of a continuous film of the same thickness is

$$V_{cont} = h\left(s+b\right)^2 \tag{0.2}$$

If the true V_2O_3 volume in the film has the same density as in bulk (ρ_{bulk}), then the effective density (ρ_{eff}) in V_2O_3 film is

$$\rho_{eff} = \rho_{bulk}\frac{V_{film}}{V_{cont}} \tag{0.3}$$

From reflectivity we can measure the electronic scattering length density (eSLD) which is proportional to density (eSLD ~ ρ_{eff}). We can define the ratio of film to bulk density (using 1.1-1.3) as

$$\phi = \frac{\rho_{eff}}{\rho_{bulk}} = \frac{V_{film}}{V_{cont}} = \frac{s^2 + s\left(b-w\right) + \frac{1}{4}\left(b-w\right)^2}{\left(s+b\right)^2} \tag{0.4}$$

X-ray reflectivity measurements show $\phi = 0.94$.

We can solve (1.4) for w

$$w = 2s\left(1-\sqrt{\phi}\right) + b\left(1-2\sqrt{\phi}\right) \tag{0.5}$$

The ratio of the uncovered substrate (ξ) area can be found with

$$\xi = \frac{w\left(2s+b-w\right)+w^2}{\left(s+b\right)^2} \tag{0.6}$$

Plugging (1.5) into (1.6)

$$\xi = \frac{(2s+b)\left(2s+b-2(b+s)\sqrt{\phi}\right)}{(s+b)^2} \tag{0.7}$$

The only poorly known parameter is *b* (grain boundary width) and we use it as a free parameter. We fit *b*= 6.37 nm (we would normally estimate b ~ 10nm). Plugging in value *s*= 100 nm, *b* = 6.37 nm (free parameter), ϕ = 0.94 we get ξ = 0.002

B.2. Reduced in-plane pressure before kink

We can model the densification of the film under hydrostatic pressure in the following way. Al_2O_3 is subject to true hydrostatic pressure, while V_2O_3 feels an out of plane pressure equal to hydrostatic pressure and a reduced in-plane pressure. When the pressure increases from 0 to 500 MPa, the uncovered area shrinks to 0 and the V_2O_3 starts to feel the normal hydrostatic pressure. The condition when all of the uncovered area disappears can be expressed as

$$\Delta A_{V2O3} = \Delta A_{Al2O3} + A_u \tag{0.8}$$

where A_u is the uncovered area at 0 pressure, and ΔA_{v2o3} and ΔA_{al2o3} are the changes in areas of V_2O_3 and Al_2O_3 respectively. The changes in areas are

$$\Delta A_{V2O3} = (x_{v2o3} + \Delta x_{v2o3})^2 - x_{v2o3}{}^2 \approx 2x_{v2o3}\Delta x_{v2o3} \tag{0.9}$$

$$\Delta A_{Al2O3} \approx 2x_{Al2o3}\Delta x_{Al2o3} \tag{0.10}$$

The uncovered area is

$$A_u = \xi x_{Al2o3}{}^2 \tag{0.11}$$

The relation between 0 pressure V_2O_3 and Al_2O_3 length scale

$$x_{v2o3} = x_{al2o3}\sqrt{(1-\xi)} \tag{0.12}$$

Plugging (1.9-1.12) into (1.8) we get

$$
\begin{aligned}
2x_{v2o3}\Delta x_{v2o3} &= 2x_{Al2o3}\Delta x_{Al2o3} + \xi x_{al2o3}{}^{2} \\
2\left(1-\xi\right)\frac{\Delta x_{v2o3}}{x_{v2o3}} &= 2\frac{\Delta x_{Al2o3}}{x_{Al2o3}} + \xi \\
2\left(1-\xi\right)\varepsilon_{v2o3,inplane} &= 2\varepsilon_{Al2o3,inplane} + \xi
\end{aligned}
\tag{0.13}
$$

where ε is the strain.

The strains can be computed from elastic tensor, assuming isotropic elastic properties

$$
c_{v2o3} = \frac{1}{E_{v2o3}}\begin{pmatrix} 1 & -\nu_{v2o3} & -\nu_{v2o3} \\ -\nu_{v2o3} & 1 & -\nu_{v2o3} \\ -\nu_{v2o3} & -\nu_{v2o3} & 1 \end{pmatrix} \tag{0.14}
$$

$$
c_{al2o3} = \frac{1}{E_{Al2o3}}\begin{pmatrix} 1 & -\nu_{Al2o3} & -\nu_{Al2o3} \\ -\nu_{Al2o3} & 1 & -\nu_{Al2o3} \\ -\nu_{Al2o3} & -\nu_{Al2o3} & 1 \end{pmatrix} \tag{0.15}
$$

Where ν are the Poisson ratios and E are the Young's modulus.

The hydrostatic stress is

$$
\sigma_{hydro} = -p_0\begin{pmatrix} 1 \\ 1 \\ 1 \end{pmatrix} \tag{0.16}
$$

and the reduced stress is

$$
\sigma_{red} = -\begin{pmatrix} p_0 \\ p_{red} \\ p_{red} \end{pmatrix} \tag{0.17}
$$

Then

$$
\begin{aligned}
\varepsilon_{V2O3} &= c_{v2o3}\sigma_{v2o3} \\
\varepsilon_{Al2O3} &= c_{Al2o3}\sigma_{Al2O3}
\end{aligned}
\tag{0.18}
$$

Combining (1.13)-(1.18) we get that at applied pressure of p_k = 500 MPa we have

$$E_{Al2O3}(\xi E_{V2O3} + 2p_{red}(1-\xi)(1-\nu_{v2o3})) + 2p_k(-E_{V2O3} + 2E_{V2O3}\nu_{Al2o3} + E_{AL2O3}(\xi-1)\nu_{v2o3}) = 0$$

(0.19)

Solving for p_{red} we get

$$p_{red} = \frac{-\xi E_{Al2O3}E_{V2O3} + 2p_k(E_{V2O3}(1-2\nu_{Al2o3}) - E_{Al2O3}(\xi-1)\nu_{v2o3})}{2E_{Al2O3}(\xi-1)(\nu_{v2o3}-1)} \quad (0.20)$$

Plugging in $\xi = 0.002$, p_k=500 MPa, and literature values for other constants we get p_{red}= 91.6 MPa. This means that the reduced in-plane pressure is almost 5 times lower than the applied hydrostatic pressure.

B.3. Ratio of slopes before and after kink

We assume that $dT_c/dP \sim dl/dP \sim d\,V^{1/3}/dP$ where V is s volume length scale (this translates the assumption that the critical temperature is linearly related to lattice constant). This can be justified by the fact that Tc changes linearly with pressure. The change in lattice constant between 0 pressure and 500 MPa (where the kink in dT/dP occurs) is:

$$l_{v2o3\,pk} = l_0\,((1 + \varepsilon_{v2o3,inplane})^2(1 + \varepsilon_{v2o3,oop}))^{1/3} \quad (1.21)$$

where l_0 is the length scale at 0 pressure (since we are taking ratios l_0 will fall out of the calculations). After the clamping pressure is reached further deformation is done with hydrostatic pressure so for applied pressure p_a and the kink pressure p_k we have

$$\varepsilon_{v2o3,clamped} = \varepsilon_{v2o3,pk} - \sigma_{v2o3}\cdot\begin{pmatrix} p_a - p_k \\ p_a - p_k \\ p_a - p_k \end{pmatrix} \quad (0.21)$$

The change in length is then analogous to 1.21

$$l_{clamped} = l_0((1+\varepsilon_{V2O3,clamped,inplane})^2(1+\varepsilon_{V2O3,clamped,outofplane}))^{1/3}$$
$$\Delta l_{clamped} = l_{clamped} - l_{v2o3,pk}$$

(0.22)

By computing $l_{clamped}$ for $P=2p_k$ we can compute the ratio $(dl/dP)_{unclamped}/(dl/dP)_{clamped} = 2.19$. Experimentally, the change in slope $(dT_c/dP)_{before\ kink}/(dT_c/dP)_{after\ kink} = 3.25$, about 48% larger than our model predicts.

B.4. Acknowledgements

This appendix was published as supplemental material for the paper Ilya Valmianski, Juan Gabriel Ramirez, Christian Urban, Xavier Batlle, and Ivan K. Schuller "Deviation from bulk in the pressure-temperature phase diagram of V2O3 thin films" Phys. Rev. B 95, 155132 (2017). The work in this appendix was done entirely by Ilya Valmianski.